# Terahertz Dirac hyperbolic metamaterial

Zhengtianye Wang<sup>1,2</sup>, Saadia Nasir<sup>3</sup>, Sathwik Bharadwaj<sup>4</sup>, Yongchen Liu<sup>1</sup>, Sivakumar Vishnuvardhan Mambakkam<sup>1</sup>, Mingyu Yu<sup>1</sup>, Stephanie Law<sup>1,2,3,5\*</sup>

- 1. Department of Materials Science and Engineering, University of Delaware, Newark, DE, 19716, U.S.A.
- 2. Two-Dimensional Crystal Consortium, Pennsylvania State University, University Park, PA, 16802, U.S.A.
- 3. Department of Physics and Astronomy, University of Delaware, Newark, DE, 19716, U.S.A.
- 4. Birck Nanotechnology Center, School of Electrical and Computer Engineering, Purdue University, West Lafayette, IN, 47907, U.S.A.
- 5. Department of Materials Science and Engineering, Pennsylvania State University, University Park, PA, 16802, U.S.A.

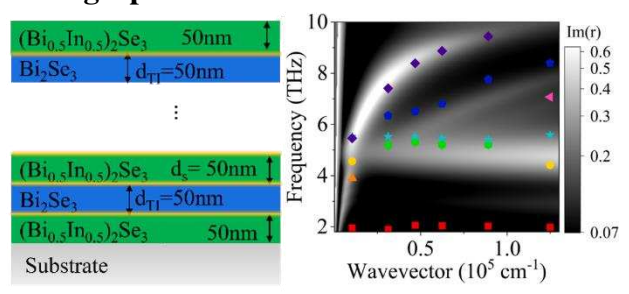
\*Corresponding author: sal6149@psu.edu

#### Abstract

Hyperbolic metamaterials (HMMs) are engineered materials with a hyperbolic isofrequency surface, enabling a range of interesting phenomena and applications including negative refraction, enhanced sensing, and subdiffraction imaging, focusing, and waveguiding. Existing HMMs primarily work in the visible and infrared spectral range due to the inherent properties of their constituent materials. Here, we demonstrate a THz-range Dirac HMM using topological insulators (TIs) as the building blocks. We find that the structure houses up to three high-wavevector volume plasmon polariton (VPP) modes, consistent with transfer matrix modeling and effective medium theory calculations. The VPPs have mode indices greater than 100, significantly larger than observed for VPP modes in HMMs made from metals or doped semiconductors while maintaining comparable quality factors. We attribute these properties to the two-dimensional Dirac nature of the electrons occupying the topological insulator surface states. Because these are van der Waals materials, these structures can be grown at a wafer-scale on a variety of substrates, allowing them to be integrated with existing THz structures and enabling next-generation THz optical devices.

**Keywords**: terahertz, metamaterial, topological insulator

# **TOC** graphic



#### Introduction

Hyperbolicity in solid material optics is of significant interest as it allows one to beat the diffraction limit and paves the way for subdiffraction imaging and waveguiding, negative refraction, enhanced sensing, and other unusual optical behavior. <sup>1-11</sup> When light propagates inside hyperbolic media, the iso-frequency surface is a hyperboloid. In these materials, the wavevector k of light that can propagate can be extremely large. Hyperbolic materials exist in nature<sup>12–19</sup>; the origin of the optical anisotropy can include phonon resonances, anisotropic effective masses, and so on. However, natural hyperbolic materials are difficult to tune as it is hard to change their inherent physical properties unless the material is ferroelectric or piezoelectric, or unless strain or changes in temperature are applied. <sup>18</sup> Fortunately, there also exist artificial hyperbolic metamaterials (HMMs) comprising subwavelength metal and dielectric components such as metal nanowires embedded in a dielectric matrix or a superlattice of alternating metal and dielectric layers<sup>11,20</sup>. HMMs overcome the tunability issue since the optical properties of the entire system can be modified by tailoring the components, including the type of the metal or dielectric, the optical component geometry (layer thickness or nanowire diameters), the metal-dielectric ratio, and so on. These materials act as effective media with anisotropic permittivities in which either the parallel or perpendicular component of the permittivity is negative while the other is positive, leading to the aforementioned hyperbolic isofrequency surface. The hyperbolicity in layered HMMs arises from the coupling of surface plasmon polaritons at every metal/dielectric interface. These coupled modes go by a variety of

names including bulk plasmon polaritons, $^{21-23}$  multilayer plasmons, $^{24}$  and volume plasmon polaritons (VPPs); $^{8,25-29}$  we will adopt the latter terminology. These VPP modes are high-k bulk cavity modes that comprise the hyperbolic isofrequency surface. They can slow light and increase light-matter interactions, and they are the foundation of subdiffraction imaging, focusing, and waveguiding $^{30}$ .

HMMs have been explored in the visible and near-infrared ranges using materials like gold, Al<sub>2</sub>O<sub>3</sub>, Si, TiO<sub>2</sub>, and perovskites, and in the mid-infrared with heavily doped III-V semiconductors<sup>26–28,31–39</sup>. However, despite the many applications, HMMs are rarely investigated in the far-infrared or terahertz (THz) ranges due to a lack of suitable materials. Fortunately, Dirac materials with a high density of states in two dimensions (2D) and low loss like graphene and topological insulators (TIs) are promising as THz HMMs<sup>40</sup>. These HMMs function through the coupling of 2D surface plasmon polaritons to create the VPP modes that form the hyperbolic isofrequency surface. Dirac HMMs based on graphene have been theoretically investigated for a variety of applications, including as biosensors, switchable reflection modulators, terahertz emitters with large Purcell effect, perfect absorbers, and super resolution lenses<sup>5,6,29,41–46</sup>. However, fabricating such structures at a wafer scale is challenging<sup>47</sup>, since the graphene typically must be transferred one layer at a time which is not truly scalable<sup>48</sup>. The direct growth of a graphene multilayer structure is even more challenging due to the difficulty of growing graphene at a wafer scale on a suitable dielectric material. On the other hand, HMMs based on topological insulators (TI) can be readily grown at a wafer scale with molecular beam epitaxy (MBE). 49-55 A TI is a topological state of matter with 2D massless conducting surface states at the boundaries between the TI and any topologically-trivial material. The plasmons polaritons in a TI exist at every interface, comprise Dirac electrons, are 2D and massless, and in general, are in the mid-infrared and THz range<sup>56–70</sup>. In a superlattice comprising alternating TI and trivial band insulator layers, topological surface states hosting Dirac plasmon polaritons emerge at each interface. If the TI and band insulator layers are thin enough, these plasmon polaritons can couple to each other, forming VPP modes and resulting in a Dirac HMM<sup>71–73</sup>.

In this paper, we report effective medium theory modeling, transfer matrix numerical simulations, and experimental evidence for VPP modes in a superlattice made of the TI Bi<sub>2</sub>Se<sub>3</sub> and the structurally-compatible trivial band insulator (Bi<sub>0.5</sub>In<sub>0.5</sub>)<sub>2</sub>Se<sub>3</sub> (BIS)<sup>74,75</sup>. We grow the multilayer film via MBE and fabricate micro-ribbon structures to couple the light and excite the VPP modes within the system. The dispersion of the VPP modes can be mapped out by analyzing the peaks in the extinction spectra as a function of ribbon width. The experimental dispersion of the VPP modes in our samples matches that predicted by semi-classical transfer matrix method modeling as well as those predicted by effective medium theory. Finally, we find that the VPP modes show mode indices 10-100x greater than those found in traditional HMMs with comparable quality factors. This experimental demonstration of VPP modes in a Dirac metamaterial showcases the richness of this TI-based system. The ability to grow this structure at the wafer scale makes it feasible for future large-scale THz-based applications. Because these structures are built from van der Waals materials, they can be grown on a variety of substrates and integrated with existing THz emitters, detectors, or other optoelectronic structures leading to new, efficient, on-chip THz devices<sup>76,77</sup>.

#### **Results and Discussion:**

The multilayer structure used in the study is shown in **Figure 1(a)**. We use BIS as the buffer layer, capping layer, and spacer layers. Ten topologically-protected surface states are expected to exist within the five-periods of 50 nm Bi<sub>2</sub>Se<sub>3</sub> and 50 nm BIS. With a thick enough spacer and high enough band offset, these surface states are quantum-mechanically uncoupled but electromagnetically coupled.<sup>60,78</sup> The extent of evanescent tail of the topological surface states (TSS) can be defined as

$$\xi = \frac{\hbar v_F}{\Delta},$$

where,  $v_F$  is the Fermi velocity, and  $\Delta$  is the bandgap at the  $\Gamma$  point. For Bi<sub>2</sub>Se<sub>3</sub>,  $v_F = 6 \times 10^5 \text{ ms}^{-1}$  and  $\Delta = 0.28 \text{ eV}$ , giving  $\xi = 14 \text{ nm}$ . Hence, for the spacer 50 nm considered

here, the TSS are quantum mechanically decoupled and the plasmon coupling will only arise through the electrostatic interaction. We will refer to this structure as '5L-50nm'. We first investigate the polariton dispersion using transfer matrix modeling. The color plot in **Figure 1(b)** presents the modeling of the 5L-50nm structure, assuming that each topological surface state has a chemical potential  $\mu$ =0.28 eV and a carrier lifetime  $\tau$ =1 ps. Below 10 THz, we see one bright branch with a dimmer and almost linearly dispersed branch below it. The brightest branch is the first VPP mode (VPP0) and the second branch is the second VPP mode (VPP1), as labeled in **Figure 1(b)**. The VPP2 mode appears as another dim linear branch at an even lower frequency which is difficult to see. The bright horizontal dispersionless mode near 4.7 THz corresponds to the epsilon near zero (ENZ) mode of BIS<sup>60</sup> which we will elaborate on in the following. An ENZ mode is a polaritonic mode that arises in materials when their permittivity is near zero. <sup>79–86</sup> The VPP modes in this region have a group velocity  $d\omega/dk > 0$ , so the HMM is classified as type II. In the 10-21 THz region, we see many branches with group velocity  $d\omega/dk < 0$ , corresponding to a type I HMM.

We have used several assumptions in the modeling. First, the BIS permittivity is obtained from fitting transmission spectra of thick films on sapphire in the 1.5-8 THz range where the sapphire is transparent; we have extrapolated its permittivity to the 8-21 THz range for the model<sup>60</sup>. Second, we used a constant permittivity for silicon across this entire frequency window. The results of the TMM modeling of the 5L-50 nm structure on silicon are close to the results of modeling on sapphire shown in the **Supporting Information**. This indicates that the hyperbolicity of the structure is due to the Bi<sub>2</sub>Se<sub>3</sub> and BIS layered structure rather than any interaction with the substrate.

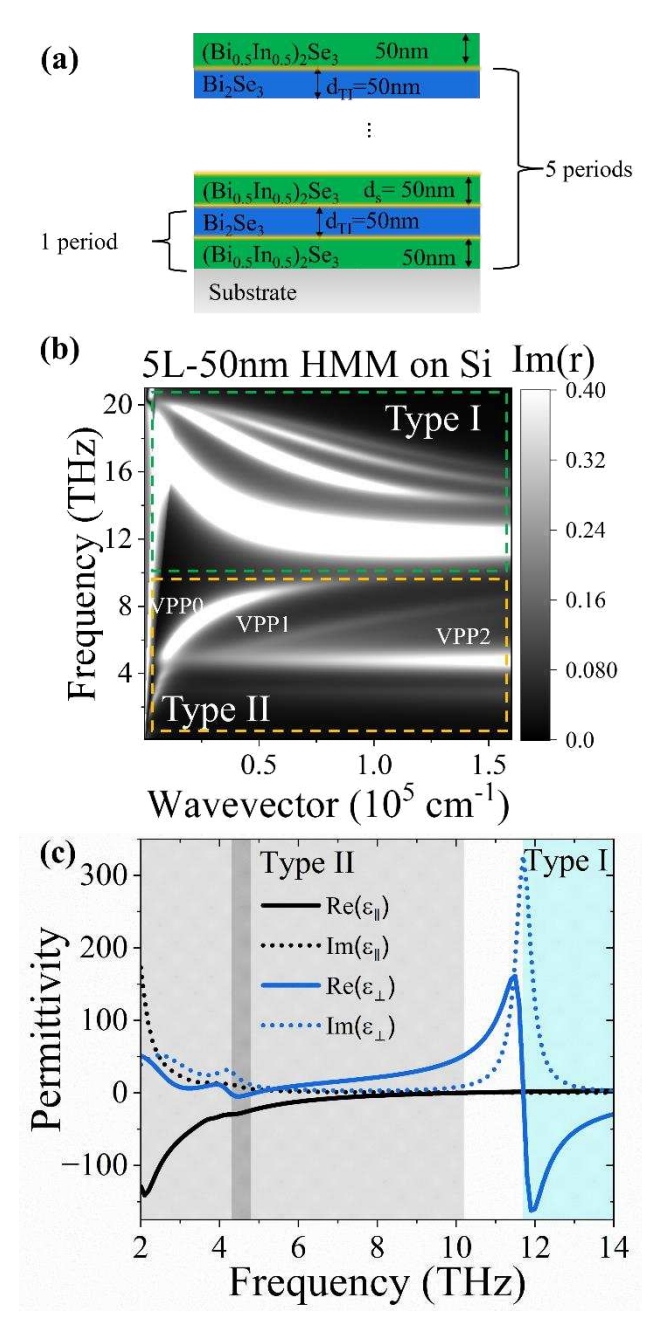


**Figure 1** (a) Schematic of the 5L-50nm multilayer HMM structure comprising five pairs of Bi<sub>2</sub>Se<sub>3</sub> and BIS with an extra BIS capping layer. (b) Transfer matrix modeling of the 5L-50nm Bi<sub>2</sub>Se<sub>3</sub>-BIS HMM. The color plot shows the imaginary part of the Fresnel reflection coefficient calculated for the structure. In the range of 1-9 THz, the structure behaves as a type II HMM, with first volume plasmon polariton (VPP0), second volume plasmon polariton (VPP1), and third volume plasmon polariton (VPP2) existing in the range of 5-9 THz. The non-dispersive mode near 5 THz is the epsilon-near-zero (ENZ) mode of BIS. In the range of 9-20 THz, the structure acts as a type I HMM. (c) Effective medium theory (EMT) modeling of the real (solid) and imaginary (dotted) parts of the parallel (black) and perpendicular (blue) components of the effective permittivity of the multilayer structure. In the gray shaded region, the structure acts like a Type II HMM, while in the blue shaded region, it acts like a Type I HMM. There is a narrow

region shaded in dark gray where both components of the permittivity are negative and the structure acts like a metal.

We can also use effective medium theory to model the structure. Details of the modeling are given in the **Supporting Information**, but in brief, we use the Maxwell-Garnett framework<sup>10</sup> to homogenize a multilayer structure. The effective parallel and perpendicular permittivities for this structure are

$$\mathcal{E}_{\parallel}(\omega) = \eta_{Bi_2Se_3} \mathcal{E}_{Bi_2Se_3} + \eta_{BIS} \mathcal{E}_{BIS} \tag{1}$$

$$\mathcal{E}_{\perp}(\omega) = \frac{\mathcal{E}_{Bi_2Se_3}\mathcal{E}_{BIS}}{\eta_{Bi_2Se_3}\mathcal{E}_{BIS} + \eta_{BIS}\mathcal{E}_{Bi_2Se_3}} \tag{2}$$

where  $\mathcal{E}_{Bi_2Se_3}$  is the frequency-dependent permittivity in the Bi<sub>2</sub>Se<sub>3</sub> layers,  $\mathcal{E}_{BIS}$  is the frequencydependent permittivity in the bottom BIS layer,  $\eta_{Bi_2Se_3}$  is the filling fraction of the Bi<sub>2</sub>Se<sub>3</sub> layers, and  $\eta_{BIS}$  is the filling fraction of the BIS layers. The Bi<sub>2</sub>Se<sub>3</sub> permittivity includes contributions from the alpha phonon, the beta phonon, and the 2D topological surface electrons, while the BIS permittivity includes the alpha and beta phonons as described in Ref. 60 and in the Supporting **Information**. The resulting effective permittivities for the entire structure are plotted in **Figure 1(c)** where the solid black line represents Re( $\mathcal{E}_{\parallel}(\omega)$ ), the dotted black line represents  $\operatorname{Im}(\mathcal{E}_{\parallel}(\omega))$ , the solid blue line represents  $\operatorname{Re}(\mathcal{E}_{\perp}(\omega))$ , and the dotted blue line represents  $\operatorname{Im}(\mathcal{E}_{\perp}(\omega))$ . These effective permittivities are clearly distinct from the permittivities of the individual Bi2Se3 and BIS layers, as shown in Figure S5 in the Supporting Information. From 2 THz to ~10.2 THz,  $\operatorname{Re}\left(\mathcal{E}_{\parallel}(\omega)\right) < 0$  while  $\operatorname{Re}\left(\mathcal{E}_{\perp}(\omega)\right) > 0$ , putting the sample in the Type II HMM regime. From ~11.7 THz to 14 THz,  $\operatorname{Re}\left(\mathcal{E}_{\parallel}(\omega)\right) > 0$  while  $\operatorname{Re}\left(\mathcal{E}_{\perp}(\omega)\right) < 0$ , putting the sample in the Type I HMM regime. There is a narrow band of frequencies from 4.3 THz to 4.8 THz where both components of the effective permittivity are negative. The results from effective medium theory match the results from the transfer matrix model reasonably well. There is a small discrepancy in the onset of the Type I regime which may be caused by the homogenization process, but the Type II regime of interest matches well. We can use the EMT model to explore

the effect of the number of periods on the optical properties of the structure. We find that the requirement Real( $\varepsilon_{\perp}$ ) > 0 is met for structures with 1-8 periods within the intended frequency range of 5 to 10 THz. However, the frequency range that satisfies Real( $\varepsilon_{||}$ ) < 0 expands as the number of periods increases and converges to the range 5-10 THz after five periods. Hence, we selected the period five as the optimal choice for our samples. Modeling details can be found in **Figure S10** in the **Supporting Information**.

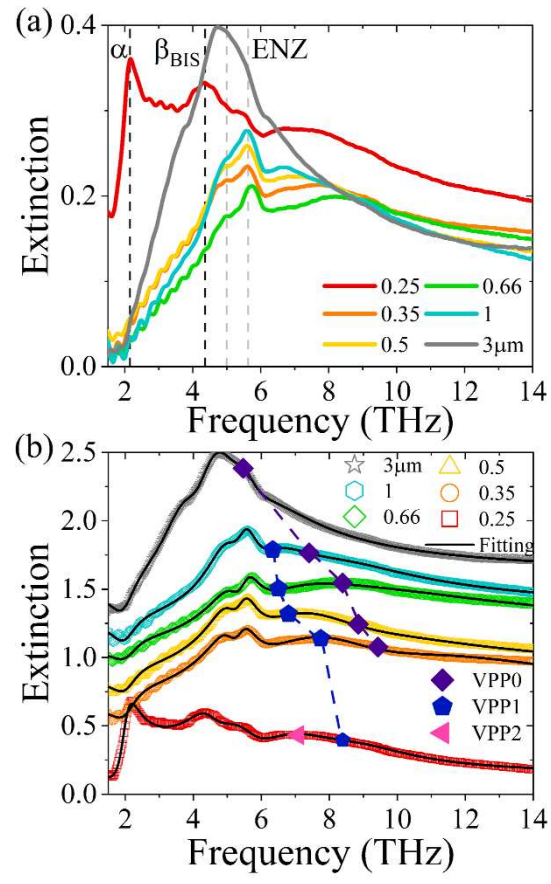


**Figure 2** (a) Transverse magnetic (TM) extinction spectra for the 5L-50nm HMM on silicon with ribbon widths from 0.25  $\mu m$  to 3  $\mu m$ . The black dashed lines mark the  $\alpha$  and  $\beta$  phonons. The grey dashed lines mark the BIS epsilon-near-zero (ENZ) modes. (b) Fitting curves for the TM extinction spectra of the 5L-50nm HMM grown on silicon. The data are multiplied by 3 and offset for better visualization. The VPP0 and VPP1 mode frequencies are marked with purple diamonds and blue pentagons, respectively. VPP2 is marked with a pink triangle. The dashed lines are a guide to the eye.

We will investigate the VPP modes in the Type II region where the high-resistivity silicon substrate is sufficiently transparent. After the films are grown using MBE, they are patterned into periodic micro-ribbon arrays using standard photolithography and etching techniques to support the excitation of the VPP modes with large wavevector (for details, see **Methods**). The polariton wavevectors are given by  $k=\pi/a$ , where a is the width of the ribbon. Extinction spectra are measured using Fourier transform infrared spectroscopy; only TM-polarized light will excite the VPP modes. By varying the ribbon widths from 3  $\mu$ m to 0.25  $\mu$ m, we can map the polariton dispersion. The extinction curves of these samples are shown in **Figure 2(a)**.

We first look at the extinction of the sample with  $a=3 \mu m$ , shown as the gray curve. The most intense peak is centered around 4.7 THz with two kinks on each side at about 3.8 THz and 6.1 THz, respectively. The peak is attributed to the VPP mode absorption while the kinks are the result of the Fano interaction between the VPP mode and the β phonon or the BIS epsilon-nearzero (ENZ) mode. A Fano interaction happens when a dispersive continuum state (for example, a VPP mode) strongly interacts with non-dispersive states with a narrow linewidth (for example, a phonon). 87,88 This interaction results in an asymmetric extinction curve. In these samples, there is also a Fano interaction between the VPP mode(s) and the  $\alpha$  phonon, which typically appears near 2 THz and is clearly visible in the TE-polarized extinction spectra (see the Supporting Information). The strong interaction has caused the peak associated with the  $\alpha$  phonon to shift to frequencies below 2 THz where the FTIR has poor sensitivity. The missing α phonon peak at 2 THz may be an indicator that a plasmon polariton mode has been excited in this type of sample, though it is not conclusive evidence. Comparing the a=3 µm sample to the others, we see that the peak around 4.7 THz is much more intense than in the other samples. We attribute this to the overlap in frequency of VPP0 and the BIS ENZ mode. In the other samples, the VPP0 mode moves away from the BIS ENZ mode, thus we no longer observe an especially intense peak.

In samples with ribbon width a=1, 0.66, 0.5, 0.35  $\mu$ m (cyan, green, yellow, and orange curves), a prominent narrow peak at around 5.5 THz accompanied by a kink around 5.0 THz are attributed to the BIS ENZ modes (indicated by gray dashed lines). The permittivity of BIS crosses zero once at the first ENZ point ( $\omega_{\text{ENZ1}} \approx 5.2 \text{ THz}$ ) and again at the second ENZ point ( $\omega_{\text{ENZ2}} \approx 5.5 \text{ THz}$ ). These ENZ modes are observable when the wavevector in the sample is relatively large. For the sample with ribbon width a=3  $\mu$ m, it is difficult to resolve the ENZ modes since the VPP mode is brighter and overlaps them in frequency. The same ENZ modes are also observed in the 5L-50 nm HMM fabricated on sapphire (see **Supporting Information**). For these samples, the VPP mode has shifted to higher frequencies and is visible as a broad peak. When the ribbon width decreases to a=0.25  $\mu$ m (red curve), the VPP mode shifts to even higher frequency, allowing the phonon peak at 2 THz to reemerge. This is caused by a decrease in the coupling strength between the VPP mode and the  $\alpha$  phonon due to the larger frequency detuning as well as the decrease in strength of the VPP mode itself. In addition, a phonon peak near 4.3 THz appears which can be attributed to the BIS  $\beta$  phonon.

In general, we see that the VPP mode peak for these samples first blue shifts (1  $\mu$ m to 0.66  $\mu$ m), then red shifts (0.66  $\mu$ m to 0.5  $\mu$ m), then blue shifts again (0.5 to 0.35  $\mu$ m). This is inconsistent with the expected dispersion from a single VPP mode and indicates the presence of multiple VPP modes. To extract the mode frequencies from the extinction curves, we employ the analytical Fano model described in the **Methods**. We use a five-oscillator model to fit the data over the range of 1.8-14 THz. One oscillator always describes the  $\alpha$  phonon. Based on the features of the curve, two oscillators are used either to describe both BIS ENZ modes (for a=1, 0.66, 0.5, 0.35  $\mu$ m), to describe one Bi<sub>2</sub>Se<sub>3</sub>  $\beta$  phonon and one ENZ mode (for a=3  $\mu$ m), or to describe one BIS  $\beta$  phonon and one ENZ mode (for a=0.25  $\mu$ m). The remaining two oscillators describe VPP modes with frequencies varying from 4 to 10 THz. As shown in **Figure 2(b)**, the fitting curves and experimental data match well. In the **Supporting Information**, we demonstrate that five oscillators are needed and rule out the possibility of a single VPP mode in

these samples. From the fitting, we can extract the VPP mode frequencies. These are shown as solid purple diamonds, blue pentagons, or pink triangles in **Figure 2(b)**; the dashed lines are a guide to the eye. For the a=0.25  $\mu$ m sample, the best fit was found when including the VPP2 mode. Since we only have one data point for VPP2 and it is relatively weak, we will exclude it from further analysis, though it will be included in the figures since it was needed for fitting.

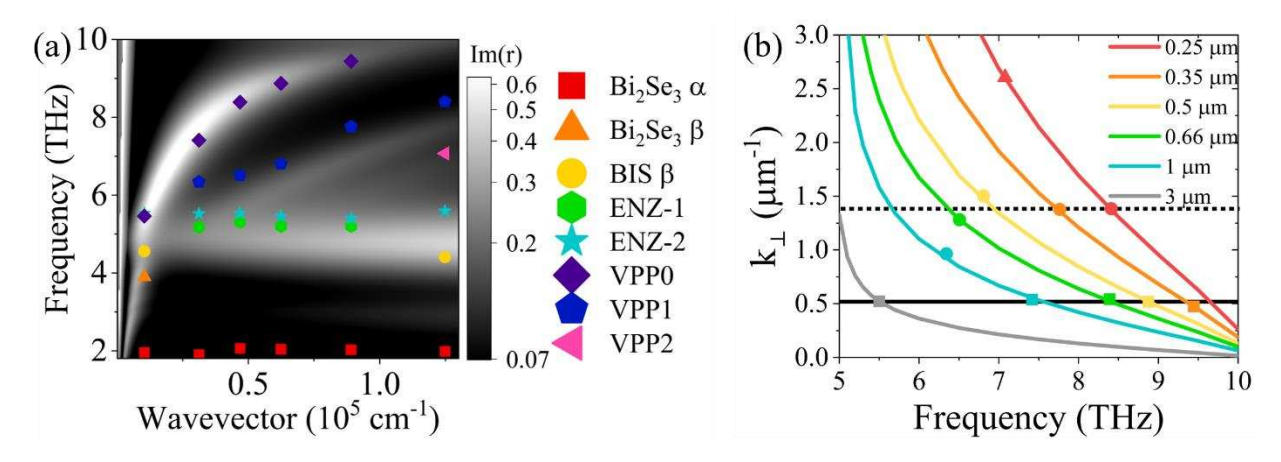


**Figure 3** (a) Transfer matrix modeling of the 5L-50nm Bi<sub>2</sub>Se<sub>3</sub>-BIS HMM shown in grayscale. Data points are the corresponding mode frequencies extracted from the fitting. (b) HMM wavevector in the perpendicular (out-of-plane) direction as a function of frequency. Solid colored lines are the predicted wavevectors from EMT; solid symbols are the experimental data points. The solid black line is the effective out-of-plane wavevector for the VPP0 mode and the dotted black line is the effective out-of-plane wavevector for the VPP1 mode.

In **Figure 3(a)**, we show the transfer matrix modelling results in grayscale. On top of this plot, we overlay the frequencies of all five oscillators used in the modeling. In every sample, we see an oscillator matching the  $\alpha$  phonon indicated by a red square. Its frequency varies in a narrow range from 1.90 to 2.06 THz which matches the clear  $\alpha$  phonon peak present in the TE extinction spectra shown in the **Supporting Information**. In most samples, we see peaks matching the VPP0 (purple diamond) and VPP1 modes (blue pentagon) as well as the ENZ-1 and ENZ-2 modes (green hexagon and cyan star, respectively). Finally, we occasionally see the  $\beta$  phonons associated with the Bi<sub>2</sub>Se<sub>3</sub> and BIS layers (orange triangle and yellow circle, respectively). We see a good agreement between the many VPP0 and VPP1 data points and the

predicted dispersion curves. The VPP1 mode deviates slightly from its predicted position at small wavevectors, which may be due to an interaction with the nearby ENZ modes which is not captured in the TMM model. As noted above, we only have one VPP2 data point (pink triangle), and it is a relatively weak mode, so we exclude it from this analysis. It is shown on this figure for completeness.

In **Figure 3(b)**, we compare our experimental data to the EMT predictions. If our material is acting like an HMM, it will have a hyperbolic isofrequency surface whose equation is given by

$$\frac{k_{\perp}^2}{\mathcal{E}_{\parallel}(\omega)} + \frac{k_{\parallel}^2}{\mathcal{E}_{\perp}(\omega)} = \frac{\omega^2}{c^2} \tag{3}$$

where  $\mathcal{E}_{\parallel}(\omega)$  and  $\mathcal{E}_{\perp}(\omega)$  are given by **Eqs. 1** and **2** using EMT and  $k_{\parallel} = \frac{1}{W}$  where W is the stripe width.<sup>58</sup> We can rewrite this equation to solve for  $k_{\perp}$ :

$$k_{\perp} = \sqrt{\mathcal{E}_{\parallel}(\omega) \left[ \frac{\omega^2}{c^2} - \frac{k_{\parallel}^2}{\mathcal{E}_{\perp}(\omega)} \right]} \tag{4}$$

In **Figure 3(b)**, the colored lines plot **Eq. 4** using the EMT expressions for  $\mathcal{E}_{\parallel}(\omega)$  and  $\mathcal{E}_{\perp}(\omega)$ . The different colors correspond to different stripe widths and thus different values for  $k_{\parallel}$ . The solid symbols represent the experimental data points corresponding to VPP0 (squares), VPP1 (circles), and VPP2 (triangle). These points were placed on the line corresponding to their stripe width at the plasmon mode frequencies determined by the fitting. For example, the sample with a stripe width of 0.35  $\mu$ m had VPP modes at 7.76 THz and 9.44 THz, as noted in the **Supporting Information**. Points were placed on the orange curve at 7.76 THz and 9.44 THz with the  $k_{\perp}$  value determined by the orange curve. Experimentally,  $k_{\perp}$  is set by the sample thickness:  $k_{\perp} = \frac{(\nu+1)}{t}$  where  $\nu$  is the mode order (0, 1, 2, ...). Given that  $k_{\perp}$  is determined by the sample thickness, if the EMT model accurately reflects our sample, we expect all of the experimental data points for a specific mode to fall along a horizontal line. This is clearly the case for VPP0, where all five points lie along the line  $k_{\perp} = 0.53 \ \mu m^{-1}$ , denoted by the horizontal solid black line. For VPP1, the data points generally lie along the line  $k_{\perp} = 1.39 \ \mu m^{-1}$ , denoted by the

horizontal dotted black line. However, the data points at lower frequencies deviate from this line. As with the TMM model, this may be caused by an interaction between the VPP1 mode and the ENZ mode that is not captured in the EMT model. These discrepancies may also be caused by finite size effects, since the experimental structure only has five periods with layers of finite thickness and EMT inherently assumes a thick sample with infinitely thin layers. However, the agreement between the experimental data and the EMT predictions is reasonable, further supporting the idea that this structure is acting like an HMM.

We can now compare the  $k_{\perp}$  values we get from **Figure 3** with those we would expect based on the film thickness. The total film thickness is 550 nm, so we would expect  $k_{\perp}^{(0)}$  $0.9 \ \mu m^{-1}$ , and  $k_{\perp}^{(1)} = 1.81 \ \mu m^{-1}$ . We see some discrepancies for VPP1 (1.39  $\mu m^{-1}$  vs.  $1.81 \, \mu m^{-1}$ ) and VPP0 (0.53  $\mu m^{-1}$  vs.  $0.9 \, \mu m^{-1}$ ). This is likely due to the electric field of the VPP mode "leaking out" of the sample. The experimental  $k_{\perp}$  values are all smaller than the prediction based on the sample thickness, corresponding to a longer real-space wavelength and a more weakly-confined mode. This effect has previously been theoretically discussed and was found to be much stronger for VPP0 and VPP1 than for the higher-order modes,<sup>22</sup> which aligns with our results. It is also possible that the effective width of the stripes is narrower than their physical width. Because the stripes are made by ion milling, the edges are likely damaged, narrowing the effective stripe width. This would have the effect of shifting the curves in **Figure 3(b)** up and to the right (e.g. the 0.66 μm curve would shift toward the 0.5 μm curve and so on). Because the frequencies of the experimental data points are fixed, this would shift the data points to larger values of  $k_{\perp}$  and closer to the theoretical prediction. Despite the discrepancy in the experimental and theoretical values of  $k_{\perp}$ , the fact that the VPP0 and VPP1 points lie on horizontal lines in **Figure 3(b)** and are easily within a factor of 2 of the theoretical  $k_{\perp}$  implies that the EMT is a reasonable model of the permittivity of the structure, and that this structure is acting like a Type II HMM.

In addition to polariton frequencies, the fitting also allows us to obtain the linewidths of these modes. For the VPP modes in the 5L-50nm sample grown on Si, the linewidths vary from

0.8-3.7 THz as shown in Table S1 in the Supporting Information. This somewhat broad linewidth contributes to the difficulty of distinguishing the two separate VPP modes. The corresponding quality factors (Q) of the VPP modes (defined as the mode frequency divided by its linewidth) range from 2.19-6.7, as shown in **Table 1**. It is likely that with decreasing temperature and/or an improvement in material quality, the carrier lifetime and thus the VPP mode lifetime will lengthen, reducing the linewidth of these modes and increasing their quality factor. Quality factors in hyperbolic metamaterials containing traditional metallic layers or doped semiconductor layers are similar (Q<20), while those found materials supporting hyperbolic phonon polaritons can be much higher (Q>250). 17,30,89-91 Naturally hyperbolic materials, however, have optical properties set by their phonons and lack the tunability of artificial HMMs. Finally, we can calculate the effective index  $(n^*)$  of the VPP modes, which is a measure of how well they confine light and is critical for applications such as subdiffraction focusing and sensing. The effective index is defined as the wavevector of the mode in the metamaterial divided by the wavevector of light in free space at the resonant frequency. We observe mode indices ranging from 126 to 531. This can be compared to artificial HMMs comprising metal or doped semiconductor layers, which have mode indices less than ~20, or to natural hyperbolic materials based on phonon polaritons, which typically have mode indices ~200. <sup>17,30,89–91</sup> These results indicate that this Dirac HMM can confine light significantly better than artificial HMMs made from traditional materials while maintaining comparable quality factors and the tunability in properties associated with artificial HMMs. These mode indices are robust to small variations in modeling. For example, if a VPP mode frequency were actually 8 THz instead of 7 THz, the mode index would be 469, while if it were actually 6 THz, the mode index would be 625. Thus, even if the model is not perfect, it is reasonable to claim that these materials house modes with very large effective indices. The large mode indices may be attributable to the two-dimensional nature of the surface plasmon polaritons that comprise the VPP modes. The fact that the material can maintain an acceptable quality factor with large mode indices may be due to the reduction in back-scattering for the electrons occupying the spin-polarized TI surface states.

**Table 1.** Mode indices (n\*) and quality factors (Q) for the VPP modes of the 5L-50nm HMM on Si

	VP	PP0	VPP1		
a (µm)	n*	Q	n*	Q	
3	55	6.7	-	-	
1	126	3.22	147	4.40	
0.66	167	2.25	215	2.19	
0.5	211	3.17	276	2.52	
0.35	283	2.56	345	2.44	
0.25	-	-	445	3.98	

#### Conclusion

In conclusion, we have excited and explored the properties of VPP modes in a five-layer TI/BI superlattice. The existence of these modes in combination with an effective medium theory model indicates that this structure is acting like a Dirac HMM in the THz spectral range. The VPP modes in these structures have mode indices 10-100x larger than those found in HMMs made from traditional materials with comparable quality factors. In the future, the position and dispersion of the VPP modes could be tuned by adjusting the material structural parameters or through gating the TI layers, unlike natural hyperbolic materials which are difficult to tune. It may also be possible to include these materials as components in topological photonic systems and metamaterials. P2.93 These large mode indices combined with the fact that these structures can be grown on a variety of substrates by van der Waals epitaxy opens the door to the creation of new types of integrated, on-chip optical and optoelectronic devices in the THz spectral range including on-chip sensors or hyperlenses to enable subdiffraction imaging.

#### Methods

**Epitaxial growth:** The Bi<sub>2</sub>Se<sub>3</sub>/BIS multilayer structures were grown on 1 cm×1 cm silicon (111) substrates via MBE using a Veeco GenXplor system. The substrate (MTI Corp.) is first cleaned via the RCA cleaning process (for details, see Supporting Information) and immediately baked at 200 °C in the load lock for 12 hours under high vacuum. After being transferred to the growth chamber (base pressure<10<sup>-9</sup> Torr), a 1×1 surface reconstruction is observed in the reflection high energy electron diffraction (RHEED) pattern with blurry diffraction streaks. The substrate is further cleaned by flashing it to 900 °C with ramp rate of 70 °C/min to obtain a clearer RHEED pattern, then cooled to 100 °C for deposition. Dual zone Knudson effusion cells are used for bismuth (UMC Corp., 6N purity grade), and indium (UMC Corp., 7N purity grade) sources. For the selenium cracking cell (UMC Corp., 6N purity grade), the base temperature is kept between 280-290°C while the cracker zone kept at 900°C. The bismuth bulk base temperature ranges from 470 °C-490 °C, depending on the growth rate needed. The cell tip temperature is kept 25 °C higher than the bulk temperature to prevent condensation near the tip. Similarly, the indium bulk temperature ranges from 670 °C-690 °C, and the tip temperature is kept 100 °C higher. The substrate is held by a rotating manipulator and temperatures are measured by a non-contact thermocouple. The Bi<sub>2</sub>Se<sub>3</sub> layers are grown at a substrate temperature of 325 °C and the BIS layers are grown at a substrate temperature of 300 °C. A selenium to bismuth flux ratio (defined by beam equivalent pressure as measured by a thoria coated iridium filament) or selenium to bismuth plus indium flux ratio is kept at 70 to maintain stoichiometry of the film. Details of the growth are included in the Supporting Information. After the final layer is grown, the sample is cooled to 200 °C in a selenium flux before being transferred out of the growth chamber. The films were stored in a vacuum pack to await measurement and fabrication. The growth process on sapphire was identical, except the substrate was heated to 650°C in the chamber before growth to desorb any contamination.

**Ribbon Fabrication.** To fabricate the micro-ribbon structures, we used electron-beam lithography (EBL) and argon ion milling. We used AR-P 6200.09 resist (Allresist, DE) with a

thickness of 200nm. The narrowest ribbon width used in this project was 250nm; the filling ratio was always 50%. After the e-beam exposure (base dose:  $200 \,\mu\text{C/cm}^2$ ) and development (developer: AR600-546), the samples were etched with argon ion milling. The remaining resist was removed by soaking the etched samples in N-Methyl-2-Pyrrolidone (NMP) in a hot water bath at 80°C for an hour. The samples were then rinsed with acetone and isopropanol and dried with nitrogen gas.

**FTIR measurement.** The extinction spectra of these samples were measured the day after nanofabrication using a Bruker Vertex 70v FTIR. The extinction of the sample is calculated as  $E=1-T/T_0$ , where T is the transmission of the sample, and  $T_0$  is the transmission of the substrate. Both transverse magnetic (TM) spectra and transverse electric (TE) spectra were measured. For TM measurements, the electric field is perpendicular to the ribbons while for TE measurements, the electric field is parallel to the ribbons. The spectra are taken with 1 cm<sup>-1</sup> (0.03 THz) resolution and a 1.6 kHz scan rate. The TM spectra are based on an average of 10000 scans while the TE spectra are based on an average of 5000 scans.

**Fano Fitting:** To obtain the VPP modes frequencies and linewidths, we use the analytical Fano resonance model to describe the interactions between non-dispersive phonons, BIS epsilon-near-zero (ENZ) modes and the VPP modes using the following equations:

Extinction(
$$\omega$$
) = 1 – T( $\omega$ ) =  $|e(\omega)|^2$  (1)

$$e(\omega) = a_r - \sum_j e_j(\omega)$$
 (2)

$$e_{j}(\omega) = \frac{b_{j}\Gamma_{j}e^{i\varphi_{j}}}{\omega - \omega_{j} + i\Gamma_{j}}$$
(3)

In these equations,  $a_r$  is the background constant,  $e(\omega)$  is the overall polarizability of the studied system, and we describe the  $j_{th}$  resonator with frequency  $\omega_j$ , linewidth  $\Gamma_j$ , phase  $\varphi_j$ , and amplitude  $b_i$ . In this model, the term  $|e_j(\omega)|^2$  describes the behavior of an isolated oscillator while the term

 $e_i(\omega)e_j(\omega)$   $i \neq j$  gives the coupling between them. The TM-polarized data from 1.5 to 14 THz are used for the fitting process. The Fano fitting is programmed using the NonlinearModel Fit embedded in Wolfram Mathematica. All of the oscillator parameters  $\omega_j$ ,  $\Gamma_j$ ,  $\varphi_j$ ,  $b_j$ , and  $a_r$  are the fitting parameters, while extinction and frequency  $\omega$  are the variables. Some constraints are used for the fitting: for example, the  $\alpha$  phonon frequency  $\omega_{\alpha}$  was constrained to lie within 1.8 THz  $<\omega_{\alpha}<$  2.3 THz, the lower and upper limit defined by the  $\alpha$  phonon frequency of pure Bi<sub>2</sub>Se<sub>3</sub> and BIS respectively. All the fittings in the main text have residual squares R>0.9995.

Transfer Matrix Modeling: A transfer matrix method is used to model the optical properties of the heterostructure. The permittivities of Bi<sub>2</sub>Se<sub>3</sub> and BIS are modeled with a Lorentz model; numerical values are given in the Supporting Information Section IX. The silicon substrate is modeled as semi-infinite with a constant permittivity  $\varepsilon_{Si}$ =11.7. The surface states are modeled as infinitely thin conducting interfaces with conductivity given by:  $\sigma$ =i $\mu$ /4 $\pi$ ( $\omega$ +i $\tau$ -1). Here  $\mu$ =0.28eV is the chemical potential of the surface state electrons which is determined by the measured electron sheet density of 1.2×10<sup>13</sup> cm<sup>-2</sup> for a 50 nm Bi<sub>2</sub>Se<sub>3</sub> film grown on a BIS buffer. We take  $\tau$ =1 ps. In electrical transport measurement, this carrier lifetime corresponds to a mobility of  $\mu_m$ =10<sup>4</sup> cm<sup>2</sup>/(V·s).

#### **Funding Sources**

Z.W., S.N., and S. L. acknowledge funding from U.S. Department of Energy, Office of Science, Office of Basic Energy Sciences, under Award No. DE-SC0017801. Y.L. acknowledges funding from UD-CHARM, a National Science Foundation MRSEC, under Award No. DMR-2011824. S.V.M. acknowledges funding from the National Science Foundation, Division of Materials Research, under Award No. 1838504. M.Y. acknowledges support from the II-VI Foundation Block Grant Program. The authors acknowledge the use of the Materials Growth Facility (MGF) at the University of Delaware, which is partially supported by the National Science Foundation Major Research Instrumentation under Grant No. 1828141 and UD-CHARM, a National Science Foundation MRSEC, under Award No. DMR-2011824.

**Supporting Information** 

Supporting Information Available: Contains growth details including substrate preparation steps

and molecular beam epitaxy growth, atomic force microscopy images of ribbon arrays,

transverse electric polarized data for the 5L-50 nm sample on silicon, details of the effective

medium theory model, experimental data fitting attempts using only four oscillators, substrate

transmission data, tables of fitting parameters, details of the material permittivity models, and

data for a similar structure grown on a sapphire substrate. This material is available free of

charge via the Internet at http://pubs.acs.org.

Author contributions: Z.W. and S.L. conceived the idea, designed the experiment, and wrote

and revised the manuscript. Z.W. carried out the material growth, nanofabrication, FTIR

measurements, data analysis, and transfer matrix modeling. S.N., Y.L., and S.V.M. assisted with

nanofabrication and structural characterization. S.B. performed the effective medium theory

calculations. M.Y. assisted with substrate preparation and atomic force microscopy confirmation

of ribbon widths. S.L. supervised the project. All authors discussed the results and commented

on the manuscript.

**Competing interests:** The authors declare no competing interests.

**References:** 

(1) Liu, Z.; Lee, H.; Xiong, Y.; Sun, C.; Zhang, X. Far-Field Optical Hyperlens Magnifying Sub-Diffraction-Limited Objects. Science 2007, 315, 1686.

(2) Lu, D.; Liu, Z. Hyperlenses and Metalenses for Far-Field Super-Resolution Imaging. *Nat. Commun.* 

**2012**, *3*, 1205. https://doi.org/10.1038/ncomms2176.

Rho, J.; Ye, Z.; Xiong, Y.; Yin, X.; Liu, Z.; Choi, H.; Bartal, G.; Zhang, X. Spherical Hyperlens for Two-Dimensional Sub-Diffractional Imaging at Visible Frequencies. Nat. Commun. 2010, 1 (9), 143.

https://doi.org/10.1038/ncomms1148.

- (4) Schwaiger, S.; Rottler, A.; Bröll, M.; Ehlermann, J.; Stemmann, A.; Stickler, D.; Heyn, C.; Heitmann, D.; Mendach, S. Broadband Operation of Rolled-up Hyperlenses. *Phys. Rev. B* **2012**, *85* (23), 235309. https://doi.org/10.1103/PhysRevB.85.235309.
- (5) Sreekanth, K. V.; De Luca, A.; Strangi, G. Negative Refraction in Graphene-Based Hyperbolic Metamaterials. *Appl. Phys. Lett.* **2013**, *103* (2), 023107. https://doi.org/10.1063/1.4813477.
- (6) Cynthia, S.; Ahmed, R.; Islam, S.; Ali, K.; Hossain, M. Graphene Based Hyperbolic Metamaterial for Tunable Mid-Infrared Biosensing. RSC Adv. 2021, 11 (14), 7938–7945. https://doi.org/10.1039/D0RA09781K.
- (7) Sreekanth, K. V.; Alapan, Y.; ElKabbash, M.; Ilker, E.; Hinczewski, M.; Gurkan, U. A.; De Luca, A.; Strangi, G. Extreme Sensitivity Biosensing Platform Based on Hyperbolic Metamaterials. *Nat. Mater.* **2016**, *15* (March), 4–11. https://doi.org/10.1038/nmat4609.
- (8) Poddubny, A.; Iorsh, I.; Belov, P.; Kivshar, Y. Hyperbolic Metamaterials. *Nat. Photonics* **2013**, *7* (12), 948–957. https://doi.org/10.1038/nphoton.2013.243.
- (9) Guo, Y.; Newman, W.; Cortes, C. L.; Jacob, Z. Applications of Hyperbolic Metamaterial Substrates. *Adv. Optoelectron.* **2012**, *2012* (1), 452502. https://doi.org/10.1155/2012/452502.
- (10) Shekhar, P.; Atkinson, J.; Jacob, Z. Hyperbolic Metamaterials: Fundamentals and Applications. *Nano Converg.* **2014**, *1* (14), 1–17. https://doi.org/10.1186/s40580-014-0014-6.
- (11) Ferrari, L.; Wu, C.; Lepage, D.; Zhang, X.; Liu, Z. Hyperbolic Metamaterials and Their Applications. *Prog. Quantum Electron.* **2015**, *40*, 1–40. https://doi.org/10.1016/j.pquantelec.2014.10.001.
- (12) Dai, S.; Ma, Q.; Liu, M. K.; Andersen, T.; Fei, Z.; Goldflam, M. D.; Wagner, M.; Watanabe, K.; Taniguchi, T.; Thiemens, M.; Keilmann, F.; Janssen, G. C. A. M.; Zhu, S. E.; Jarillo-Herrero, P.; Fogler, M. M.; Basov, D. N. Graphene on Hexagonal Boron Nitride as a Tunable Hyperbolic Metamaterial. *Nat. Nanotechnol.* 2015, 10, 682–686. https://doi.org/10.1038/nnano.2015.131.
- (13) Guo, Y.; Jacob, Z. Broadband Super-Planckian Thermal Emission from Hyperbolic Metamaterials. *Appl. Phys. Lett.* **2012**, *101*, 131106. https://doi.org/10.1364/cleo\_qels.2013.qtu3a.4.
- (14) Sun, J.; Litchinitser, N. M.; Zhou, J. Indefinite by Nature: From Ultraviolet to Terahertz. *ACS Photonics* **2014**, *1* (4), 293–303. https://doi.org/10.1021/ph4000983.
- (15) Narimanov, E. E.; Kildishev, A. V. Metamaterials: Naturally Hyperbolic. *Nat. Photonics* **2015**, *9* (4), 214–216. https://doi.org/10.1038/nphoton.2015.56.
- (16) Wu, J. S.; Basov, D. N.; Fogler, M. M. Topological Insulators Are Tunable Waveguides for Hyperbolic Polaritons. *Phys. Rev. B* **2015**, *92* (20), 205430. https://doi.org/10.1103/PhysRevB.92.205430.
- (17) Caldwell, J. D.; Kretinin, A. V.; Chen, Y.; Giannini, V.; Fogler, M. M.; Francescato, Y.; Ellis, C. T.; Tischler, J. G.; Woods, C. R.; Giles, A. J.; Hong, M.; Watanabe, K.; Taniguchi, T.; Maier, S. A.; Novoselov, K. S. Sub-Diffractional Volume-Confined Polaritons in the Natural Hyperbolic Material Hexagonal Boron Nitride. *Nat. Commun.* **2014**, *5*, 1–9. https://doi.org/10.1038/ncomms6221.
- (18) Korzeb, K.; Gajc, M.; Pawlak, D. A. Compendium of Natural Hyperbolic Materials. *Opt. Express* **2015**, *23* (20), 25406. https://doi.org/10.1364/OE.23.025406.
- (19) Caldwell, J. D.; Kretinin, A. V.; Chen, Y.; Giannini, V.; Fogler, M. M.; Francescato, Y.; Ellis, C. T.; Tischler, J. G.; Woods, C. R.; Giles, A. J.; Hong, M.; Watanabe, K.; Taniguchi, T.; Maier, S. A.; Novoselov, K. S. Sub-Diffractional Volume-Confined Polaritons in the Natural Hyperbolic Material Hexagonal Boron Nitride. *Nat. Commun.* **2014**, *5*, 5221. https://doi.org/10.1038/ncomms6221.
- (20) Kidwai, O.; Zhukovsky, S. V.; Sipe, J. E. Effective-Medium Approach to Planar Multilayer Hyperbolic Metamaterials: Strengths and Limitations. *Phys. Rev. A* **2012**, *85* (5), 053842. https://doi.org/10.1103/PhysRevA.85.053842.
- (21) Vasilantonakis, N.; Nasir, M. E.; Dickson, W.; Wurtz, G. A.; Zayats, A. V. Bulk Plasmon-Polaritons in Hyperbolic Nanorod Metamaterial Waveguides. *Laser Photonics Rev.* **2015**, *9* (3), 345–353. https://doi.org/10.1002/lpor.201400457.

- (22) Avrutsky, I.; Salakhutdinov, I.; Elser, J.; Podolskiy, V. Highly Confined Optical Modes in Nanoscale Metal-Dielectric Multilayers. *Phys. Rev. B* **2007**, *75* (24), 241402(R). https://doi.org/10.1103/PhysRevB.75.241402.
- (23) Sun, L.; Li, Z.; Luk, T. S.; Yang, X.; Gao, J. Nonlocal Effective Medium Analysis in Symmetric Metal-Dielectric Multilayer Metamaterials. *Phys. Rev. B* 2015, *91* (19), 195147. https://doi.org/10.1103/PhysRevB.91.195147.
- (24) Schilling, J. Uniaxial Metallo-Dielectric Metamaterials with Scalar Positive Permeability. *Phys. Rev. E* **2006**, *74* (4), 046618. https://doi.org/10.1103/PhysRevE.74.046618.
- (25) Ishii, S.; Kildishev, A. V.; Narimanov, E.; Shalaev, V. M.; Drachev, V. P. Sub-Wavelength Interference Pattern from Volume Plasmon Polaritons in a Hyperbolic Medium. *Laser Photonics Rev.* **2013**, *7* (2), 265–271. https://doi.org/10.1002/lpor.201200095.
- (26) Zhukovsky, S. V.; Kidwai, O.; Sipe, J. E. Physical Nature of Volume Plasmon Polaritons in Hyperbolic Metamaterials. *Opt. Express* **2013**, *21* (12), 14982–14987. https://doi.org/10.1364/OE.21.014982.
- (27) Wei, D.; Harris, C.; Law, S. Volume Plasmon Polaritons in Semiconductor Hyperbolic Metamaterials. *Opt. Mater. Express* **2017**, *7* (7), 2672–2681.
- (28) Sreekanth, K. V.; De Luca, A.; Strangi, G. Excitation of Volume Plasmon Polaritons in Metal-Dielectric Metamaterials Using 1D and 2D Diffraction Gratings. *J. Opt.* **2014**, *16* (10), 105103. https://doi.org/10.1088/2040-8978/16/10/105103.
- (29) Zhukovsky, S. V.; Andryieuski, A.; Sipe, J. E.; Lavrinenko, A. V. From Surface to Volume Plasmons in Hyperbolic Metamaterials: General Existence Conditions for Bulk High-k Waves in Metal-Dielectric and Graphene-Dielectric Multilayers. *Phys. Rev. B* **2014**, *90* (15), 155429. https://doi.org/10.1103/PhysRevB.90.155429.
- (30) Sohr, P.; Wei, D.; Tomasulo, S.; Yakes, M. K.; Law, S. Simultaneous Large Mode Index and High Quality Factor in Infrared Hyperbolic Metamaterials. *ACS Photonics* **2018**, *5* (10), 4003–4008. https://doi.org/10.1021/acsphotonics.8b01097.
- (31) Sreekanth, K. V.; De Luca, A.; Strangi, G. Experimental Demonstration of Surface and Bulk Plasmon Polaritons in Hypergratings. *Sci. Rep.* **2013**, *3*, 3291. https://doi.org/10.1038/srep03291.
- (32) Smalley, J. S. T.; Vallini, F.; Shahin, S.; Kanté, B.; Fainman, Y. Gain-Enhanced High-k Transmission through Metal-Semiconductor Hyperbolic Metamaterials. *Opt. Mater. Express* **2015**, *5* (10), 2300. https://doi.org/10.1364/OME.5.002300.
- (33) Sohr, P.; Law, S. Structural Parameters of Hyperbolic Metamaterials Controlling High-k Mode Resonant Wavelengths. *J. Opt. Soc. Am. B* **2020**, *37* (12), 3784. https://doi.org/10.1364/josab.404763.
- (34) Chandrasekar, R.; Wang, Z.; Meng, X.; Azzam, S. I.; Shalaginov, M. Y.; Lagutchev, A.; Kim, Y. L.; Wei, A.; Kildishev, A. V.; Boltasseva, A.; Shalaev, V. M. Lasing Action with Gold Nanorod Hyperbolic Metamaterials. *ACS Photonics* **2017**, *4* (3), 674–680. https://doi.org/10.1021/acsphotonics.7b00010.
- (35) Kim, J.; Drachev, V. P.; Jacob, Z.; Naik, G. V.; Boltasseva, A.; Narimanov, E. E.; Shalaev, V. M. Improving the Radiative Decay Rate for Dye Molecules with Hyperbolic Metamaterials. *Opt. Express* **2012**, *20* (7), 8100. https://doi.org/10.1364/OE.20.008100.
- (36) Naik, G. V.; Liu, J.; Kildishev, A. V.; Shalaev, V. M.; Boltasseva, A. Demonstration of Al:ZnO as a Plasmonic Component for near-Infrared Metamaterials. *Proc Natl Acad Sci* **2012**, *109* (23), 8834–8838. https://doi.org/10.1073/pnas.1121517109.
- (37) Urbas, A. M.; Jacob, Z.; Negro, L. D.; Engheta, N.; Boardman, A. D.; Egan, P.; Khanikaev, A. B.; Menon, V.; Ferrera, M.; Kinsey, N.; DeVault, C.; Kim, J.; Shalaev, V.; Boltasseva, A.; Valentine, J.; Pfeiffer, C.; Grbic, A.; Narimanov, E.; Zhu, L.; Fan, S.; Alù, A.; Poutrina, E.; Litchinitser, N. M.; Noginov, M. A.; MacDonald, K. F.; Plum, E.; Liu, X.; Nealey, P. F.; Kagan, C. R.; Murray, C. B.; Pawlak,

- D. A.; Smolyaninov, I. I.; Smolyaninova, V. N.; Chanda, D. Roadmap on Optical Metamaterials. *J. Opt.* **2016**, *18* (9), 093005. https://doi.org/10.1088/2040-8978/18/9/093005.
- (38) Li, Z.; Smalley, J. S. T.; Haroldson, R.; Lin, D.; Hawkins, R.; Gharajeh, A.; Moon, J.; Hou, J.; Zhang, C.; Hu, W.; Zakhidov, A.; Gu, Q. Active Perovskite Hyperbolic Metasurface. *ACS Photonics* **2020**, *7* (7), 1754–1761. https://doi.org/10.1021/acsphotonics.0c00391.
- (39) Basak, S.; Bar-On, O.; Scheuer, J. Perovskite/Metal-Based Hyperbolic Metamaterials: Tailoring the Permittivity Properties of Coexisting Anisotropies in the Visible Region. *Adv. Opt. Mater.* **2021**, *9* (1), 2001305. https://doi.org/10.1002/adom.202001305.
- (40) Atsushi Ishikawa, T. T. Plasmon Hybridization in Graphene Metamaterials. *Appl. Phys. Lett.* **2013**, No. 102, 253110. https://doi.org/10.1063/1.4812813.
- (41) Othman, M. A. K.; Guclu, C.; Capolino, F. Graphene-Based Tunable Hyperbolic Metamaterials and Enhanced near-Field Absorption. *Opt. Express* **2013**, *21* (6), 7614. https://doi.org/10.1364/oe.21.007614.
- (42) Iorsh, I. V.; Mukhin, I. S.; Shadrivov, I. V.; Belov, P. A.; Kivshar, Y. S. Hyperbolic Metamaterials Based on Multilayer Graphene Structures. *Phys. Rev. B Condens. Matter Mater. Phys.* **2013**, *87* (7), 075416. https://doi.org/10.1103/PhysRevB.87.075416.
- (43) Pianelli, A.; Pianelli, A.; Kowerdziej, R.; Kowerdziej, R.; Dudek, M.; Sielezin, K.; Olifierczuk, M.; Parka, J. Graphene-Based Hyperbolic Metamaterial as a Switchable Reflection Modulator. *Opt. Express* **2020**, *28* (5), 6708–6718. https://doi.org/10.1364/OE.387065.
- (44) Kozina, O. N.; Melnikov, L. A.; Nefedov, I. S. A Theory for Terahertz Lasers Based on a Graphene Hyperbolic Metamaterial. *J. Opt.* **2020**, *22* (9), 095003. https://doi.org/10.1088/2040-8986/aba678.
- (45) Xiang, Y.; Dai, X.; Guo, J.; Zhang, H.; Wen, S.; Tang, D. Critical Coupling with Graphene-Based Hyperbolic Metamaterials. *Sci. Rep.* **2014**, *4* (1), 5483. https://doi.org/10.1038/srep05483.
- (46) Nefedov, I. S.; Valagiannopoulos, C. A.; Melnikov, L. A. Perfect Absorption in Graphene Multilayers. *J. Opt.* **2013**, *15* (11), 114003. https://doi.org/10.1088/2040-8978/15/11/114003.
- (47) Lin, H.; Sturmberg, B. C. P.; Lin, K.-T.; Yang, Y.; Zheng, X.; Chong, T. K.; de Sterke, C. M.; Jia, B. A 90-Nm-Thick Graphene Metamaterial for Strong and Extremely Broadband Absorption of Unpolarized Light. *Nat. Photonics* **2019**, *13* (4), 270–276. https://doi.org/10.1038/s41566-019-0389-3.
- (48) Chang, Y.; Liu, C.; Liu, C.; Zhang, S.; Marder, S. R. Realization of Mid-Infrared Graphene Hyperbolic Metamaterials. *Nat. Commun.* **2016**, *7*, 10568. https://doi.org/10.1038/ncomms10568.
- (49) Fornari, C. I.; Rappl, P. H. O.; Morelhão, S. L.; Abramof, E. Structural Properties of Bi2Te3 Topological Insulator Thin Films Grown by Molecular Beam Epitaxy on (111) BaF2 Substrates. *J. Appl. Phys.* **2016**, *119* (16), 165303. https://doi.org/10.1063/1.4947266.
- (50) Ginley, T.; Wang, Y.; Law, S. Topological Insulator Film Growth by Molecular Beam Epitaxy: A Review. *Crystals* **2016**, *6* (11), 154. https://doi.org/10.3390/cryst6110154.
- (51) He, L.; Kou, X.; Wang, K. L. Review of 3D Topological Insulator Thin-Film Growth by Molecular Beam Epitaxy and Potential Applications. *Phys. Status Solidi RRL* **2013**, *7* (1–2), 50–63. https://doi.org/10.1002/pssr.201307003.
- (52) Liu, X.; Smith, D. J.; Fan, J.; Zhang, Y.-H.; Cao, H.; Chen, Y. P.; Leiner, J.; Kirby, B. J.; Dobrowolska, M.; Furdyna, J. K. Structural Properties of Bi2Te3 and Bi2Se3 Topological Insulators Grown by Molecular Beam Epitaxy on GaAs(001) Substrates. *Appl. Phys. Lett.* 2011, 99 (17), 171903. https://doi.org/10.1063/1.3655995.
- (53) Ginley, T.; Law, S. Growth of Bi2Se3 Topological Insulator Films Using a Selenium Cracker Source. *J. Vac. Sci. Technol. B* **2016**, *34*, 02L105. https://doi.org/10.1116/1.4941134.
- (54) Wang, Z.; Law, S. Optimization of the Growth of the Van Der Waals Materials Bi2Se3 and (Bi0.5In0.5)2Se3 by Molecular Beam Epitaxy. *Cryst. Growth Des.* **2021**, *21* (12), 6752–6765. https://doi.org/10.1021/acs.cgd.1c00663.

- (55) Wang, Y.; Ginley, T. P.; Law, S. Growth of High-Quality Bi2Se3 Topological Insulators Using (Bi1-xlnx)2Se3 Buffer Layers. *J. Vac. Sci. Technol. B* **2018**, *36*, 02D101.
- (56) Nasir, S.; Wang, Z.; Mambakkam, S. V.; Law, S. In-Plane Plasmon Coupling in Topological Insulator Bi2Se3thin Films. *Appl. Phys. Lett.* **2021**, *119* (20), 201103. https://doi.org/10.1063/5.0071895.
- (57) Pietro, P. Di; Ortolani, M.; Limaj, O.; Gaspare, A. Di; Giliberti, V.; Giorgianni, F.; Brahlek, M.; Bansal, N.; Koirala, N.; Oh, S.; Calvani, P.; Lupi, S. Observation of Dirac Plasmons in a Topological Insulator. *Nat. Nanotechnol.* **2013**, *8*, 556–560. https://doi.org/10.1038/nnano.2013.134.
- (58) Ginley, T. P.; Law, S. Coupled Dirac Plasmons in Topological Insulators. *Adv. Opt. Mater.* **2018**, *6* (13), 1800113. https://doi.org/10.1002/adom.201800113.
- (59) In, C.; Sim, S.; Kim, B.; Bae, H.; Jung, H.; Jang, W.; Son, M.; Moon, J.; Salehi, M.; Seo, S. Y.; Soon, A.; Ham, M. H.; Lee, H.; Oh, S.; Kim, D.; Jo, M. H.; Choi, H. Control over Electron-Phonon Interaction by Dirac Plasmon Engineering in the Bi2Se3 Topological Insulator. *Nano Lett.* **2018**, *18* (2), 734–739. https://doi.org/10.1021/acs.nanolett.7b03897.
- (60) Wang, Z.; Ginley, T. P.; Mambakkam, S. V.; Chandan, G.; Zhang, Y.; Ni, C.; Law, S. Plasmon Coupling in Topological Insulator Multilayers. *Phys. Rev. Mater.* 2020, 4 (11), 115202. https://doi.org/10.1103/PhysRevMaterials.4.115202.
- (61) Autore, M.; Engelkamp, H.; D'Apuzzo, F.; Gaspare, A. D.; Pietro, P. D.; Vecchio, I. L.; Brahlek, M.; Koirala, N.; Oh, S.; Lupi, S. Observation of Magnetoplasmons in Bi <sub>2</sub> Se <sub>3</sub> Topological Insulator. *ACS Photonics* **2015**, *2* (9), 1231–1235. https://doi.org/10.1021/acsphotonics.5b00036.
- (62) Autore, M.; D'Apuzzo, F.; Di Gaspare, A.; Giliberti, V.; Limaj, O.; Roy, P.; Brahlek, M.; Koirala, N.; Oh, S.; Garcia de Abajo, F. J.; Lupi, S. Plasmon-Phonon Interactions in Topological Insulator Microrings. *Adv. Opt. Mater.* **2015**, *3* (9), 1257–1263. https://doi.org/10.1002/adom.201400513.
- (63) Autore, M.; Di Pietro, P.; Di Gaspare, A.; D'Apuzzo, F.; Giorgianni, F.; Brahlek, M.; Koirala, N.; Oh, S.; Lupi, S. Terahertz Plasmonic Excitations in Bi <sup>2</sup> Se <sup>3</sup> Topological Insulator. *J. Phys. Condens. Matter* **2017**, *29* (18), 183002. https://doi.org/10.1088/1361-648X/aa63ac.
- (64) Brey, L. Plasmonics in Topological Insulators: Spin Charge Separation, the In FI Uence of the Inversion Layer, and Phonon – Plasmon Coupling. 2017. https://doi.org/10.1021/acsphotonics.7b00524.
- (65) Di Pietro, P.; Ortolani, M.; Limaj, O.; Di Gaspare, A.; Giliberti, V.; Giorgianni, F.; Brahlek, M.; Bansal, N.; Koirala, N.; Oh, S.; Calvani, P.; Lupi, S. Plasmonic Excitations in Bi 2 Se 3 Topological Insulator. *J. Phys. Condens. Matter* **2017**, *29*, 183002.
- (66) Qi, J.; Liu, H.; Xie, X. C. Surface Plasmon Polaritons in Topological Insulators. *Phys. Rev. B* **2014**, *89*, 155420. https://doi.org/10.1103/PhysRevB.89.155420.
- (67) Profumo, R. E. V.; Asgari, R.; Polini, M.; MacDonald, A. H. Double-Layer Graphene and Topological Insulator Thin-Film Plasmons. *Phys. Rev. B* 2012, 85 (8), 085443. https://doi.org/10.1103/PhysRevB.85.085443.
- (68) Efimkin, D. K.; Lozovik, Y. E. Collective Excitonic and Plasmonic Excitations on a Surface of 3D Topological Insulator. J. Phys. Conf. Ser. 2012, 393, 012016. https://doi.org/10.1088/1742-6596/393/1/012016.
- (69) Efimkin, D. K.; Lozovik, Y. E.; Sokolik, A. A. Spin-Plasmons in Topological Insulator. *J. Magn. Magn. Mater.* **2012**, *324* (21), 3610–3612. https://doi.org/10.1016/j.jmmm.2012.02.102.
- (70) Deshko, Y.; Krusin-Elbaum, L.; Menon, V.; Khanikaev, A.; Trevino, J. Surface Plasmon Polaritons in Topological Insulator Nano-Films and Superlattices. *Opt. Express* 2016, 24 (7), 7398. https://doi.org/10.1364/OE.24.007398.
- (71) Zhang, R. Z. Optical and Thermal Radiative Properties of Topological Insulator Semiconductor Multilayers. J. Quant. Spectrosc. Radiat. Transf. 2020, 253, 107133. https://doi.org/10.1016/j.jqsrt.2020.107133.

- (72) Sreekanth, K. V.; Simpson, R. E. Super-Collimation and Negative Refraction in Hyperbolic Van Der Waals Superlattices. *Opt. Commun.* 2019, 440 (February), 150–154. https://doi.org/10.1016/j.optcom.2019.02.020.
- (73) Krishnamoorthy, H. N. S.; Dubrovkin, A. M.; Adamo, G.; Soci, C. Topological Insulator Metamaterials. *Chem. Rev.* 2023, 123 (8), 4416–4442. https://doi.org/10.1021/acs.chemrev.2c00594.
- (74) Koirala, N.; Brahlek, M.; Salehi, M.; Wu, L.; Dai, J.; Waugh, J.; Nummy, T.; Han, M. G.; Moon, J.; Zhu, Y.; Dessau, D.; Wu, W.; Armitage, N. P.; Oh, S. Record Surface State Mobility and Quantum Hall Effect in Topological Insulator Thin Films via Interface Engineering. *Nano Lett.* **2015**, *15* (12), 8245–8249. https://doi.org/10.1021/acs.nanolett.5b03770.
- (75) Wang, Y.; Ginley, T. P.; Law, S. Growth of High-Quality Bi<sub>2</sub>Se<sub>3</sub> Topological Insulators Using (Bi<sub>1-xlnx</sub>)<sub>2</sub>Se<sub>3</sub> Buffer Layers Growth of High-Quality Bi<sub>2</sub>Se<sub>3</sub> Topological Insulators Using (Bi<sub>1-xlnx</sub>)<sub>2</sub>Se<sub>3</sub> Buffer Layers. *J. Vaccum Sci. Technol. B* **2018**, *36* (2), 02D101. https://doi.org/10.1116/1.5015968.
- (76) To, D. Q.; Wang, Z.; Ho, D. Q.; Hu, R.; Acuna, W.; Liu, Y.; Bryant, G. W.; Janotti, A.; Zide, J. M. O.; Law, S.; Doty, M. F. Strong Coupling between a Topological Insulator and a III-V Heterostructure at Terahertz Frequency. *Phys. Rev. Mater.* 2022, 6 (3), 035201. https://doi.org/10.1103/PhysRevMaterials.6.035201.
- (77) To, D. Q.; Wang, Z.; Liu, Y.; Wu, W.; Jungfleisch, M. B.; Xiao, J. Q.; Zide, J. M. O.; Law, S.; Doty, M. F. Surface Plasmon-Phonon-Magnon Polariton in a Topological Insulator-Antiferromagnetic Bilayer Structure. *Phys. Rev. Mater.* **2022**, *6* (8), 085201. https://doi.org/10.1103/PhysRevMaterials.6.085201.
- (78) Brahlek, M. J.; Koirala, N.; Liu, J.; Yusufaly, T. I.; Salehi, M.; Han, M. G.; Zhu, Y.; Vanderbilt, D.; Oh, S. Tunable Inverse Topological Heterostructure Utilizing (Bi1-xInx)2Se3 and Multichannel Weak-Antilocalization Effect. *Phys. Rev. B* **2016**, *93* (12), 1–5. https://doi.org/10.1103/PhysRevB.93.125416.
- (79) Wu, J.; Xie, Z. T.; Sha, Y.; Fu, H. Y.; Li, Q. Epsilon-near-Zero Photonics: Infinite Potentials. *Photonics Res.* **2021**, *9* (8), 1616–1644. https://doi.org/10.1364/PRJ.427246.
- (80) Reshef, O.; De Leon, I.; Alam, M. Z.; Boyd, R. W. Nonlinear Optical Effects in Epsilon-near-Zero Media. *Nat. Rev. Mater.* **2019**, *4* (8), 535–551. https://doi.org/10.1038/s41578-019-0120-5.
- (81) Powell, D. A.; Alù, A.; Edwards, B.; Vakil, A.; Kivshar, Y. S.; Engheta, N. Nonlinear Control of Tunneling through an Epsilon-near-Zero Channel. *Phys. Rev. B* 2009, 79 (24), 245135. https://doi.org/10.1103/PhysRevB.79.245135.
- (82) Pollard, R. J.; Murphy, A.; Hendren, W. R.; Evans, P. R.; Atkinson, R.; Wurtz, G. A.; Zayats, A. V.; Podolskiy, V. A. Optical Nonlocalities and Additional Waves in Epsilon-Near-Zero Metamaterials. *Phys. Rev. Lett.* **2009**, *102* (12), 127405. https://doi.org/10.1103/PhysRevLett.102.127405.
- (83) Niu, X.; Hu, X.; Chu, S.; Gong, Q. Epsilon-Near-Zero Photonics: A New Platform for Integrated Devices. *Adv. Opt. Mater.* **2018**, *6* (10), 1701292. https://doi.org/10.1002/adom.201701292.
- (84) Fomra, D.; Ball, A.; Saha, S.; Wu, J.; Sojib, Md.; Agrawal, A.; Lezec, H. J.; Kinsey, N. Nonlinear Optics at Epsilon near Zero: From Origins to New Materials. *Appl. Phys. Rev.* **2024**, *11* (1), 011317. https://doi.org/10.1063/5.0186961.
- (85) Fruhling, C.; Ozlu, M. G.; Saha, S.; Boltasseva, A.; Shalaev, V. M. Understanding All-Optical Switching at the Epsilon-near-Zero Point: A Tutorial Review. *Appl. Phys. B* **2022**, *128* (2), 34. https://doi.org/10.1007/s00340-022-07756-4.
- (86) Alù, A.; Silveirinha, M. G.; Salandrino, A.; Engheta, N. Epsilon-near-Zero Metamaterials and Electromagnetic Sources: Tailoring the Radiation Phase Pattern. *Phys. Rev. B* **2007**, *75* (15), 155410. https://doi.org/10.1103/PhysRevB.75.155410.

- (87) Giannini, V.; Francescato, Y.; Amrania, H.; Phillips, C. C.; Maier, S. A. Fano Resonances in Nanoscale Plasmonic Systems: A Parameter-Free Modeling Approach. *Nano Lett.* **2011**, *11* (7), 2835–2840. https://doi.org/10.1021/nl201207n.
- (88) Luk'yanchuk, B.; Zheludev, N. I.; Maier, S. A.; Halas, N. J.; Nordlander, P.; Giessen, H.; Chong, C. T. The Fano Resonance in Plasmonic Nanostructures and Metamaerials. *Nat Mater* **2010**, *9* (9), 707–715. https://doi.org/10.1038/nmat2810.
- (89) Caldwell, J. D.; Glembocki, O. J.; Francescato, Y.; Sharac, N.; Giannini, V.; Bezares, F. J.; Long, J. P.; Owrutsky, J. C.; Vurgaftman, I.; Tischler, J. G.; Wheeler, V. D.; Bassim, N. D.; Shirey, L. M.; Kasica, R.; Maier, S. A. Low-Loss, Extreme Subdiffraction Photon Confinement via Silicon Carbide Localized Surface Phonon Polariton Resonators. *Nano Lett.* 2013, 13 (8), 3690–3697. https://doi.org/10.1021/nl401590g.
- (90) Feng, K.; Harden, G.; Sivco, D. L.; Hoffman, A. J. Subdiffraction Confinement in All-Semiconductor Hyperbolic Metamaterial Resonators. *ACS Photonics* **2017**, *4* (7), 1621–1626. https://doi.org/10.1021/acsphotonics.7b00309.
- (91) Yang, X.; Yao, J.; Rho, J.; Yin, X.; Zhang, X. Experimental Realization of Three-Dimensional Indefinite Cavities at the Nanoscale with Anomalous Scaling Laws. *Nat. Photonics* **2012**, *6*, 1–24. https://doi.org/10.1038/NPHOTON.2012.124.
- (92) Hou, J.; Li, Z.; Luo, X.-W.; Gu, Q.; Zhang, C. Topological Bands and Triply Degenerate Points in Non-Hermitian Hyperbolic Metamaterials. *Phys. Rev. Lett.* **2020**, *124* (7), 073603. https://doi.org/10.1103/PhysRevLett.124.073603.
- (93) Li, Z.; Gu, Q. Topological Hyperbolic Metamaterials. *Nanophotonics* **2024**, *13* (6), 825–839. https://doi.org/10.1515/nanoph-2023-0768.
- (94) Hao, J.; Zhou, L. Electromagnetic Wave Scatterings by Anisotropic Metamaterials: Generalized 4x4 Transfer-Matrix Method. *Phys. Rev. B Condens. Matter Mater. Phys.* **2008**, *77* (9), 1–12. https://doi.org/10.1103/PhysRevB.77.094201.

# **Supporting Information for**

# Terahertz Dirac hyperbolic metamaterial

Zhengtianye Wang<sup>1,2</sup>, Saadia Nasir<sup>3</sup>, Sathwik Bharadwaj<sup>4</sup>, Yongchen Liu<sup>1</sup>, Sivakumar Vishnuvardhan Mambakkam<sup>1</sup>, Mingyu Yu<sup>1</sup>, Stephanie Law<sup>1,2,3,5\*</sup>

- 6. Department of Materials Science and Engineering, University of Delaware, Newark, DE, 19716, U.S.A.
- 7. Two-Dimensional Crystal Consortium, Pennsylvania State University, University Park, PA, 16802, U.S.A.
- 8. Department of Physics and Astronomy, University of Delaware, Newark, DE, 19716, U.S.A.
- 9. Birck Nanotechnology Center, School of Electrical and Computer Engineering, Purdue University, West Lafayette, IN, 47907, U.S.A.
- 10. Department of Materials Science and Engineering, Pennsylvania State University, University Park, PA, 16802, U.S.A.

\*Corresponding author: sal6149@psu.edu

# I. Growth of the Bi<sub>2</sub>Se<sub>3</sub> and (Bi<sub>0.5</sub>In<sub>0.5</sub>)<sub>2</sub>Se<sub>3</sub> superlattice on silicon Substrate preparation:

There is always a layer of silicon oxide on top the silicon wafer, so it is critical to remove the oxide layer before any epitaxial growth. Because the surface oxide layer on our wafer is thin (~2nm), we used an RCA clean. After removing the 1 cm×1 cm Si (111) substrate from the package, we sonicated it in acetone and isopropanol for 10min each to remove possible organic contamination. Then we dipped the wafer in a base-peroxide mixture (volume ratio: H<sub>2</sub>O:H<sub>2</sub>O<sub>2</sub> (30% by weight):NH<sub>4</sub>OH (29% by weight)=5:1:1) at 80 °C for 10 min to further remove organics and other contamination (metals, etc.) from the surface. This step is known as the first standard clean step (SC-1). The native oxide dissolves at a very low rate and a new silicon oxide layer (~1nm) regenerates at the same time at approximately the same rate. After rinsing the wafer in flowing water for 1min, we dipped the wafer in an acid-peroxide mixture (volume ratio: H<sub>2</sub>O:H<sub>2</sub>O<sub>2</sub> (30% by weight):HCl(37% by weight)=6:1:1) at 80 °C for 10 min. This second standard clean step (SC-2) removes the trace of ions introduced in SC-1. Finally, we rinse the wafer in flowing water for about 1 min, followed by drying with nitrogen flow. The wafer is immediately loaded into the molecular beam epitaxy (MBE) system load lock, which is pumped down below 10<sup>-6</sup> Torr in 2 min. The wafer is baked in the load lock at 200 °C for 12 hrs before loading into the main MBE chamber.

After loading the substrate into the growth chamber, the substrate reflection high energy electron diffraction (RHEED) pattern shows the expected 1×1 Si (111) surface reconstruction, as shown in Fig. S1(a). The substrate is the flashed to 900 °C at a 70 °C/min ramp rate to further clean the substrate. After reaching 900 °C, the substrate heater is turned off and the substrate naturally cools to 100 °C. We note that if the substrate were flashed above 950 °C in our chamber, a 7×7 surface reconstruction appears as shown in Fig. S1(b). When the substrate is cooled to around 710 °C, the Si (111) surface return to 1×1 reconstruction. To minimize the history of the substrate surface, we therefore only flash the substrate to 900 °C.

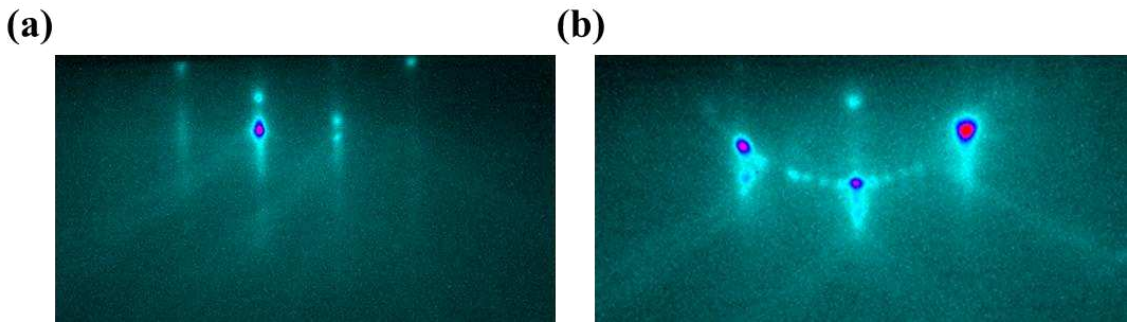


**Figure S1**. RHEED pattern of (a) 1×1 surface reconstruction and (b) 7×7 surface reconstruction on a Si (111) substrate.

# **Film Deposition:**

Before the  $Bi_2Se_3$  deposition, the substrate is exposed to a selenium flux (same beam equivalent pressure as used for the  $Bi_2Se_3$  growth step) for 1 min at 100 °C to passivate the surface dangling bonds. Then 3 nm of  $Bi_2Se_3$  are deposited at 100 °C, followed by 2 nm of  $Bi_2Se_3$  and 5 nm of  $In_2Se_3$  at 300 °C and finally 40 nm ( $Bi_{0.5}In_{0.5}$ )<sub>2</sub>Se<sub>3</sub> via co-deposition to form a buffer layer. The subsequent  $Bi_2Se_3$  and ( $Bi_{0.5}In_{0.5}$ )<sub>2</sub>Se<sub>3</sub> layers are deposited at 325 °C and 300 °C, respectively. The manipulator rotates the substrate at 2 °C/min throughout the process to maintain an even substrate temperature and deposition rate across the wafer. A 5  $\mu$ m×5  $\mu$ m atomic force microscopy image of the 5L-50nm sample is shown in Fig. S2. The root mean square roughness of the surface is 11.59nm out of a 550 nm film.

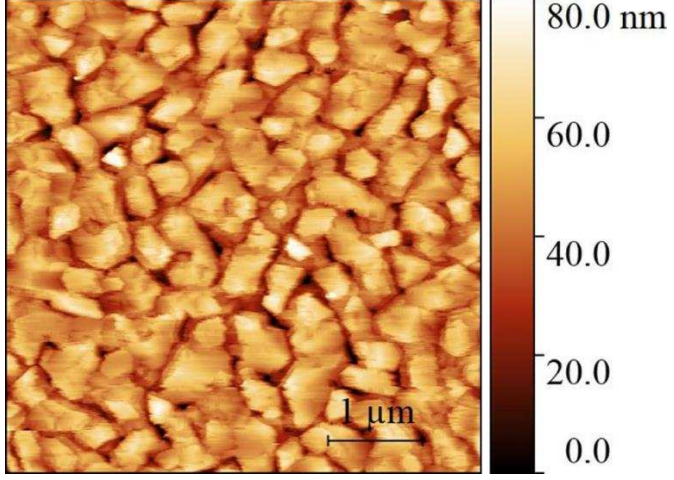


**Figure S2**. Atomic force microscopy image of the 5L-50nm  $\overline{Bi_2Se_3}$  and  $(Bi_{0.5}In_{0.5})_2Se_3$  superlattice film on Si (111), size:  $5 \mu m \times 5 \mu m$ . Taken by Veeco Dimension-3100V SPM.

# II. Atomic force microscopy images of ribbon arrays

Atomic force microscopy (AFM) images of the ribbon arrays fabricated on silicon along with their respective line cuts are shown in Fig. S3. The horizontal blue lines indicate where the line cuts were taken. For each of the line cuts, purple vertical lines are drawn to indicate the intended width of each ribbon. For the sample with the 3 $\mu$ m stripe width, we can see that the intended stripe width matches the measured stripe width well. However, as the stripes get narrower, the data becomes more difficult to resolve. For the sample with the 0.25 $\mu$ m stripe width, the stripes are almost impossible to see. This is because, as the period becomes smaller, the AFM tip width is comparable to the spacing between stripes. We are therefore seeing a convolution of the tip and sample data, making it more and more difficult to interpret the data as the stripes get narrower. However, for stripes as narrow as 0.35 $\mu$ m, the stripe width and height measured by AFM are comparable to what we designed. Data for the sample fabricated on sapphire is similar.

# AFM of HMM on Si

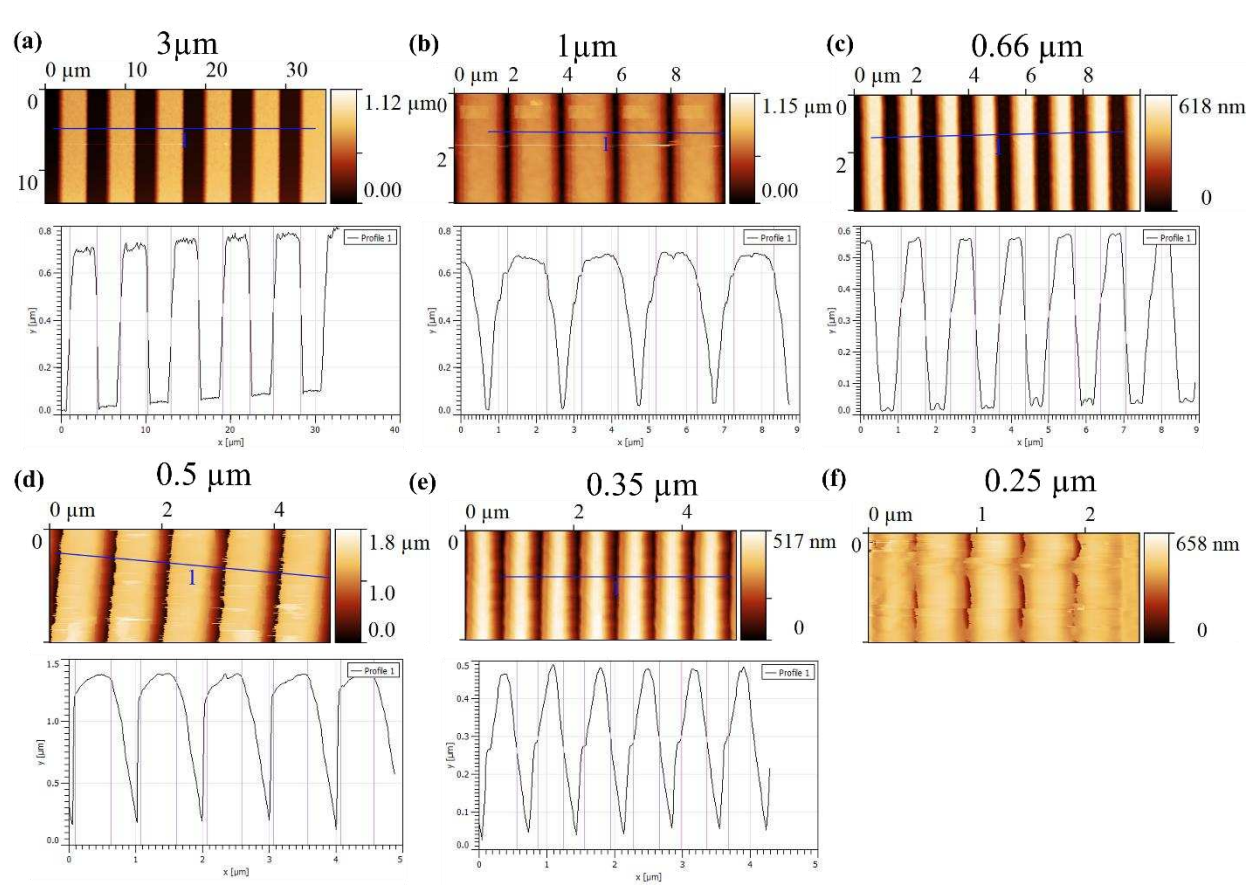


**Figure S3**. Atomic force microscopy images and line cuts of the 5L-50nm  $Bi_2Se_3$  and  $(Bi_{0.5}In_{0.5})_2Se_3$  superlattice film on Si (111) for ribbons with sizes 3  $\mu$ m (a), 1  $\mu$ m (b), 0.66 $\mu$ m (c), 0.5 $\mu$ m (d), 0.35 $\mu$ m (e), and 0.25 $\mu$ m (f). No linecut is included for (f) since the AFM tip was too wide to properly resolve the spacing between stripes.

#### III. TE data of 5L-50nm on Si

The TE spectra of the samples are shown in Fig. S4. In the TE set up, the electric field is polarized parallel to the ribbons. The extinction is defined as 1-T/T<sub>0</sub>, where T is the spectrum of the sample and T<sub>0</sub> is the substrate spectrum with the same optical set up. The TE data confirms that the samples remain the same after the nanofabrication process and that the phonons in the system are nearly the same for all six samples.

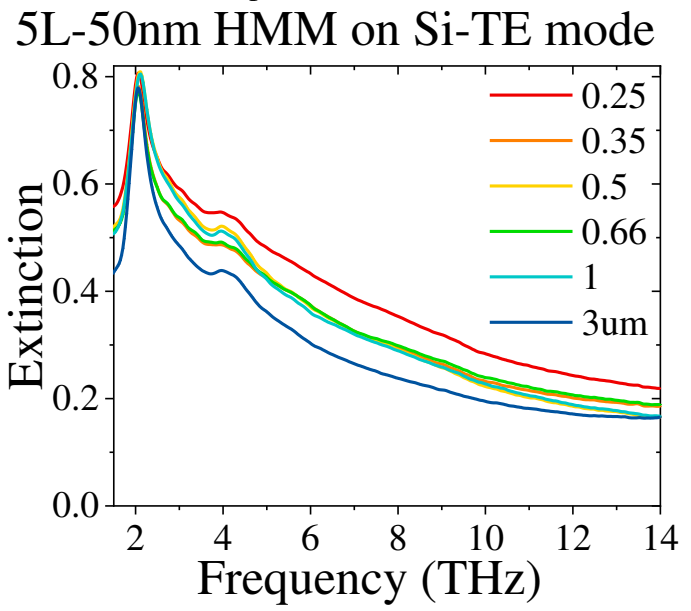


**Figure S4**. TE spectra of the 5L-50nm HMM on Si (111), measured by FTIR with 1.6 kHz scan rate and integrated over 5000 scans.

#### IV. **Effective Medium Theory Modeling**

Let us consider a Bi<sub>2</sub>Se<sub>3</sub>/(Bi<sub>0.5</sub>In<sub>0.5</sub>)<sub>2</sub>Se<sub>3</sub> (BIS) superlattice with the z-axis as the perpendicular growth direction and the x, y-axes forming the surface plane. We consider a TM polarized wave in a uniaxial medium and the isofrequency surface satisfies the relation

$$\frac{\left(q_x^2 + q_y^2\right)}{\varepsilon_{\parallel}(\omega)} + \frac{q_z^2}{\varepsilon_{\perp}(\omega)} = \frac{\omega^2}{c^2} \tag{1}$$

Where  $\vec{q} = [q_x, q_y, q_z]$  is the wavevector of a propagating wave,  $\omega$  is the frequency, c is the speed of light,  $\varepsilon_{\parallel}(\omega)$  and  $\varepsilon_{\perp}(\omega)$  are the in-plane and out-of-plane dielectric functions. The standard procedure for homogenizing a multilayer with subwavelength layer thicknesses uses the Maxwell-Garnett framework<sup>1</sup>, and the effective dielectric function for a uniaxial medium is given by

$$\varepsilon_{eff}(\omega) = \begin{pmatrix} \varepsilon_{\parallel}(\omega) & 0 & 0 \\ 0 & \varepsilon_{\parallel}(\omega) & 0 \\ 0 & 0 & \varepsilon_{\perp}(\omega) \end{pmatrix}$$
 (2)

When the dielectric function satisfies the condition Re  $(\varepsilon_{\parallel}(\omega)) \cdot \text{Re}(\varepsilon_{\perp}(\omega)) < 0$ , the isofrequency surface forms a hyperboloid. We note that the electric field and displacement field satisfy the boundary conditions:

$$E_{BIS}^{\parallel} = E_{Bi_2Se_3}^{\parallel} = E^{\parallel}$$
 (3)  
 $D_{BIS}^{\perp} = D_{Bi_2Se_3}^{\perp} = D^{\perp}$  (4)

$$D_{BIS}^{\perp} = D_{Bi_2Se_3}^{\perp} = D^{\perp} \tag{4}$$

where  $E^{\parallel}$  and  $D^{\perp}$  are the electric and displacement field components of the subwavelength metamaterial. The effective displacement field is given by

$$D = \eta_{Bi_2Se_3} E_{Bi_2Se_3} + \eta_{BIS} E_{BIS}$$
 (5)

 $D = \eta_{Bi_2Se_3} E_{Bi_2Se_3} + \eta_{BIS} E_{BIS}$  where  $\eta_{Bi_2Se_3}$  and  $\eta_{BIS}$  are the filling fractions of the Bi<sub>2</sub>Se<sub>3</sub> and BIS layers, respectively. Using the boundary conditions, we can derive the parallel and perpendicular components of the effective dielectric function given by

$$\mathcal{E}_{\parallel}(\omega) = \eta_{Bi_2Se_3} \mathcal{E}_{Bi_2Se_3} + \eta_{BIS} \mathcal{E}_{BIS} \tag{6}$$

$$\mathcal{E}_{\parallel}(\omega) = \eta_{Bi_2Se_3} \mathcal{E}_{Bi_2Se_3} + \eta_{BIS} \mathcal{E}_{BIS}$$

$$\mathcal{E}_{\perp}(\omega) = \frac{\mathcal{E}_{Bi_2Se_3} \mathcal{E}_{BIS}}{\eta_{Bi_2Se_3} \mathcal{E}_{BIS} + \eta_{BIS} \mathcal{E}_{Bi_2Se_3}}$$

$$(6)$$

where we use

$$\varepsilon_{Bi_2Se_3}(\omega) = 1 + \frac{s_\alpha^2}{\omega_\alpha^2 - \omega^2 - i\omega\gamma_\alpha} + \frac{s_\beta^2}{\omega_\beta^2 - \omega^2 - i\omega\gamma_\beta} - \frac{\omega_D^2}{\omega^2 + i\omega\gamma_D}$$
(8)

and

$$\varepsilon_{BIS}(\omega) = \varepsilon_{\infty,p} + \frac{S_{\alpha}^2}{\Omega_{\alpha}^2 - \omega^2 - i\omega\gamma_{\alpha}} + \frac{S_{\beta}^2}{\Omega_{\beta}^2 - \omega^2 - i\omega\gamma_{\beta}}$$
(9)

The subscripts  $\alpha$ ,  $\beta$ , and D here represent Lorentz oscillators assigned to the  $\alpha$  phonon, the  $\beta$ phonon, and the Drude electron contributions, respectively. Parameters for the above expressions for the dielectric function of Bi<sub>2</sub>Se<sub>3</sub> and BIS are obtained from Ref. <sup>2</sup>. In our calculations, we considered five-periods of 50nm Bi<sub>2</sub>Se<sub>3</sub> and 50nm BIS layers, and the BIS is taken as the buffer layer, capping layer, and spacer layer.

We note that for indium concentrations above x=0.06,  $(Bi_{(1-x)}In_x)_2Se_3$  is a topologicallytrivial material.<sup>3</sup> Hence, BIS here forms the band insulator layer. The 2D conducting surface states exist at the boundaries between the topological insulator Bi<sub>2</sub>Se<sub>3</sub> and the band insulator

(Bi<sub>(1-x)</sub>In<sub>x</sub>)<sub>2</sub>Se<sub>3</sub>. This contribution is included by the Drude term in Eq. (8). Conductivity measurements have shown that the dielectric response of Bi<sub>2</sub>Se<sub>3</sub> in its topological insulator state can be described by a single Drude term for free 2D electrons and two Lorentz phonon oscillator terms as shown in Eq. (8).<sup>4,5</sup> Further, the Drude term contribution is completely attributed to the topological surface states rather than the bulk-free carrier contributions. Post et al.<sup>6</sup> employed a model based on the *f*-sum rule for the linear Dirac dispersion to calculate the topological surface states contributions to the dielectric function, and showed that the experimentally measured Drude oscillator strength is well within the theoretical limit for the isolated Dirac surface states response. Further, the Drude term is experimentally shown to be thickness-independent,<sup>7</sup> hence attributing the contribution only from the topological surface states rather than the bulk contribution. In our calculations, the topological 2D conducting state contributions are included within the Drude term in Eq. (8). This contribution is crucial for the observation of Type-II and Type-I hyperbolic metamaterials behavior in a wide range of frequencies as shown in Fig. 2 in the main text.

As shown in Fig. S5, the permittivity extracted from the effective medium theory model is very different than the permittivities of the individual Bi<sub>2</sub>Se<sub>3</sub> and BIS layers.

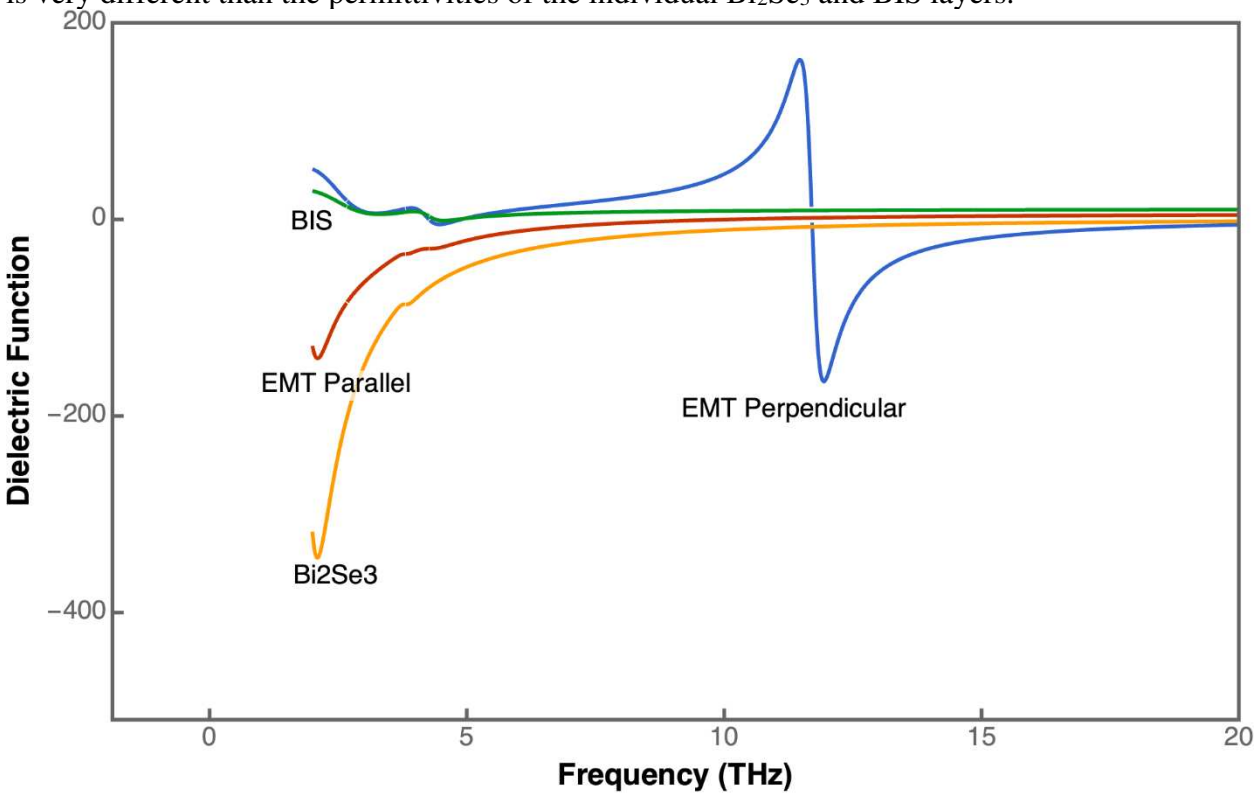


**Figure S5**. Permittivity of Bi<sub>2</sub>Se<sub>3</sub> (yellow) and BIS (green) layers compared to the effective medium theory permittivity in the parallel (red) and perpendicular (blue) directions.

Below, we have plotted below the individual contributions of  $\alpha$  phonon,  $\beta$  phonon, and topological surface state (TSS) to the dielectric function of the topological insulator layer Bi<sub>2</sub>Se<sub>3</sub>. We see that the predominant contributions to the overall dielectric function of the Bi<sub>2</sub>Se<sub>3</sub> originate from  $\alpha$  phonon and topological surface states.

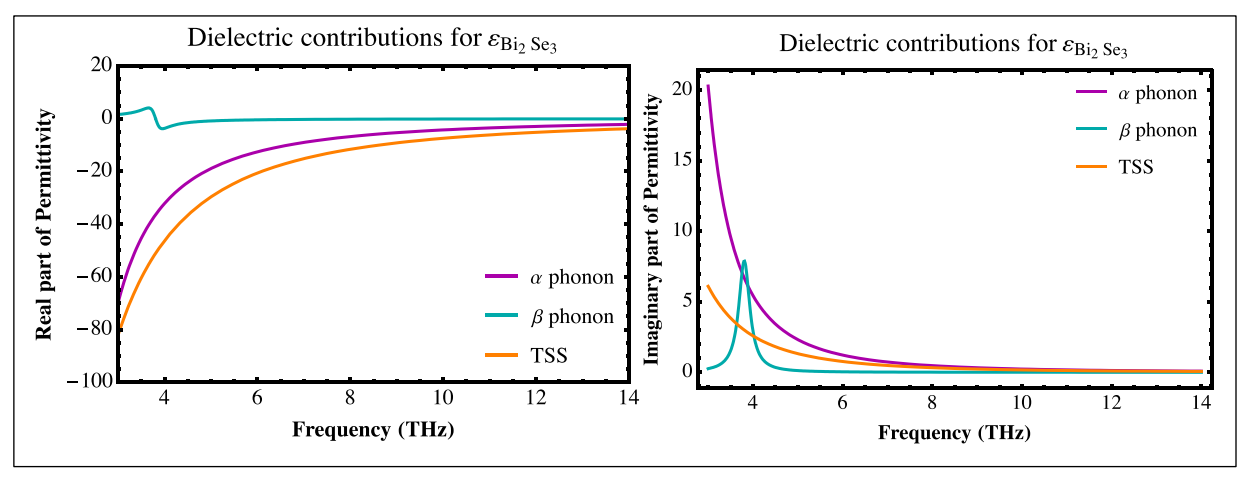


**Figure S6**. Contributions of  $\alpha$  phonon,  $\beta$  phonon, and the topological surface states to the overall dielectric function of the topological insulator layer Bi<sub>2</sub>Se<sub>3</sub>

# V. Simultaneous Four-Oscillator Fitting

Because of the similarities among the extinction curves of samples with a=1, 0.66, 0.5, 0.35 µm, we decided to see if we could adopt a simultaneous fitting procedure where we hold the  $\alpha$  phonon, ENZ1, and ENZ2 mode constant for all four sets of data and only allow the plasmon to vary. Compared to the independent four oscillators fitting where we have 4 (oscillators) ×4 ( $\omega$ j,  $\Gamma$ j,  $\varphi$ j,  $\theta$ j) =16 fitting parameters for each set of data and 16×4=64 for all 4 sets, the simultaneous fitting has reduced the fitting parameters to 3 (oscillators) ×4 (parameters  $\omega$ j,  $\Gamma$ j,  $\varphi$ j,  $\theta$ j) + 4 (parameters  $\theta$ j,  $\theta$ j,  $\theta$ j) × 4 (data sets) =28.

Fig. S7 shows the simultaneous fitting results with residual square R>0.999. Fig. S5(a-d) are the fitting curves overlaid on top of the experimental data. Good fits are observed for the samples with a=0.66 and 0.5  $\mu$ m. However, for samples with a=1 and 0.35  $\mu$ m, the one free oscillator model cannot capture the curve shape in the range of 6 to 10 THz. Furthermore, we can plot the individual oscillators  $|e_j(\omega)|^2$  in Fig. S7(e). The plasmon frequencies obtained via the simultaneous fitting are quite close to each other, in a narrow range from 6.4 to 6.8 THz, which indicates an almost non-dispersive plasmon polariton mode. The fitting result is not consistent with our TMM modeling. The four oscillators simultaneous fitting indicates that an extra free oscillator is needed to fit the TM-polarized extinction spectra.

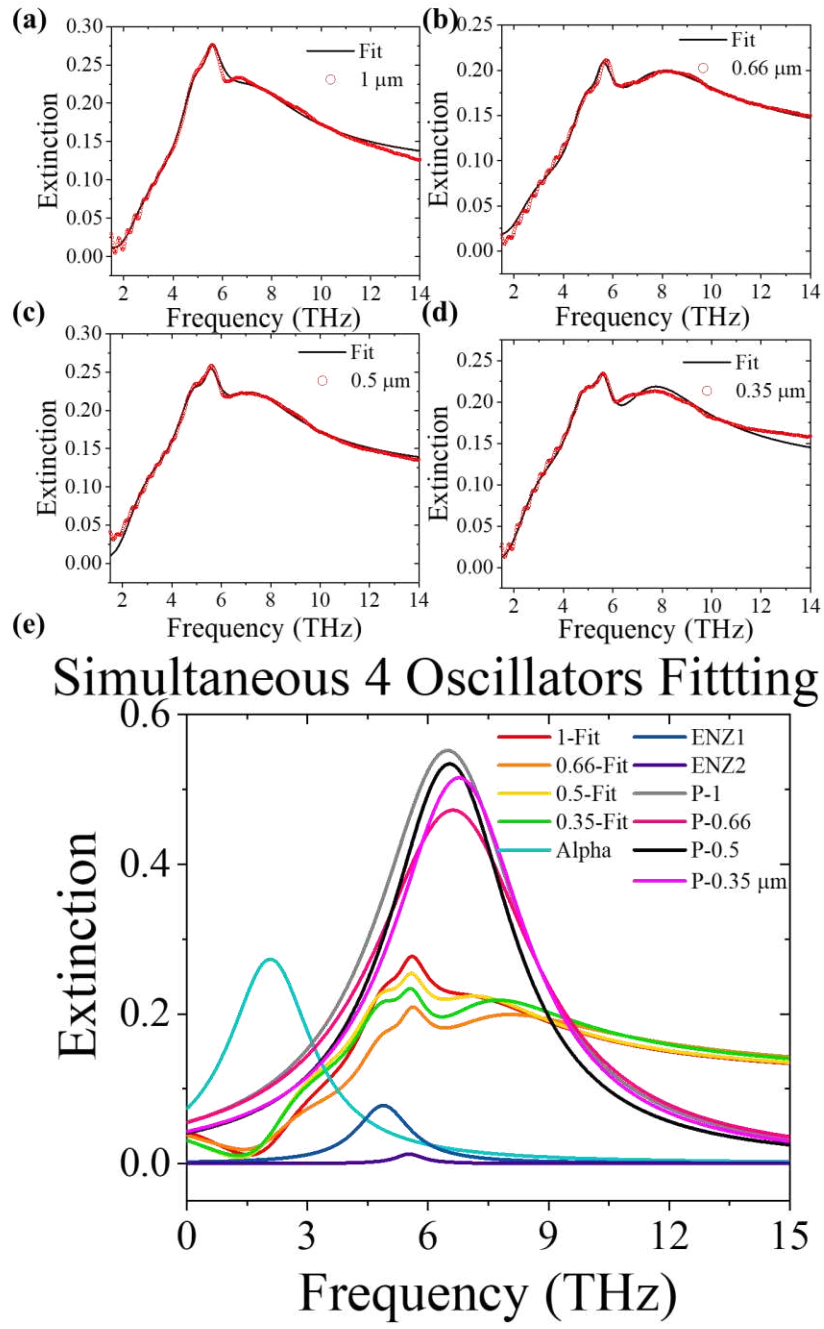


**Figure S7**. (a-d) Experimental data points (open red circles) and fitting curves (black lines) for the simultaneous four oscillator fitting for samples with ribbon widths a=1, 0.66, 0.5, 0.35  $\mu$ m, respectively. (e) Individual oscillators extracted from the fitting process. Red, orange, yellow, and green curves are the fitting curves shown in panels (a-d). Cyan, blue, and violet curves are the  $\alpha$  phonon, BIS ENZ1 mode and ENZ2 mode respectively. The gray, black, magenta, and pink curves represent the plasmon polaritons.

#### VI. Independent Four-Oscillator Fitting

Because the simultaneous fitting was unable to give satisfying fitting curves for the samples with a=1 and 0.35  $\mu$ m, we returned to the independent fitting but only used four oscillators as opposed to the five-oscillator model in the main text. Fig. S8 shows the best fitting results using this model. For the sample with a=0.35  $\mu$ m, we can get an acceptable fit with a single plasmon frequency at 6.61THz, while for the sample with a=1  $\mu$ m, the shape in the range from 6 to 8 THz is still not captured by the fitting curve (though it is better than the fitting in the simultaneous fitting process shown in Fig. S7(a)). The single plasmon frequency is at 6.17 THz. We did not do the independent fitting for the other two samples as the fitting curve in the simultaneous fitting process already matches the experimental data well. We would expect similar results coming from independent fitting.

Even with the independent four-oscillator fitting process, the plasmon frequencies are within 1THz, which is almost non-dispersive. In addition, the curve shape for the a=1  $\mu$ m sample cannot be captured using either fitting method. This indicates that the single plasmon assumption is not applicable to these samples. Thus, we adopted the five-oscillator model as described in the main text to capture the expected two plasmon modes.

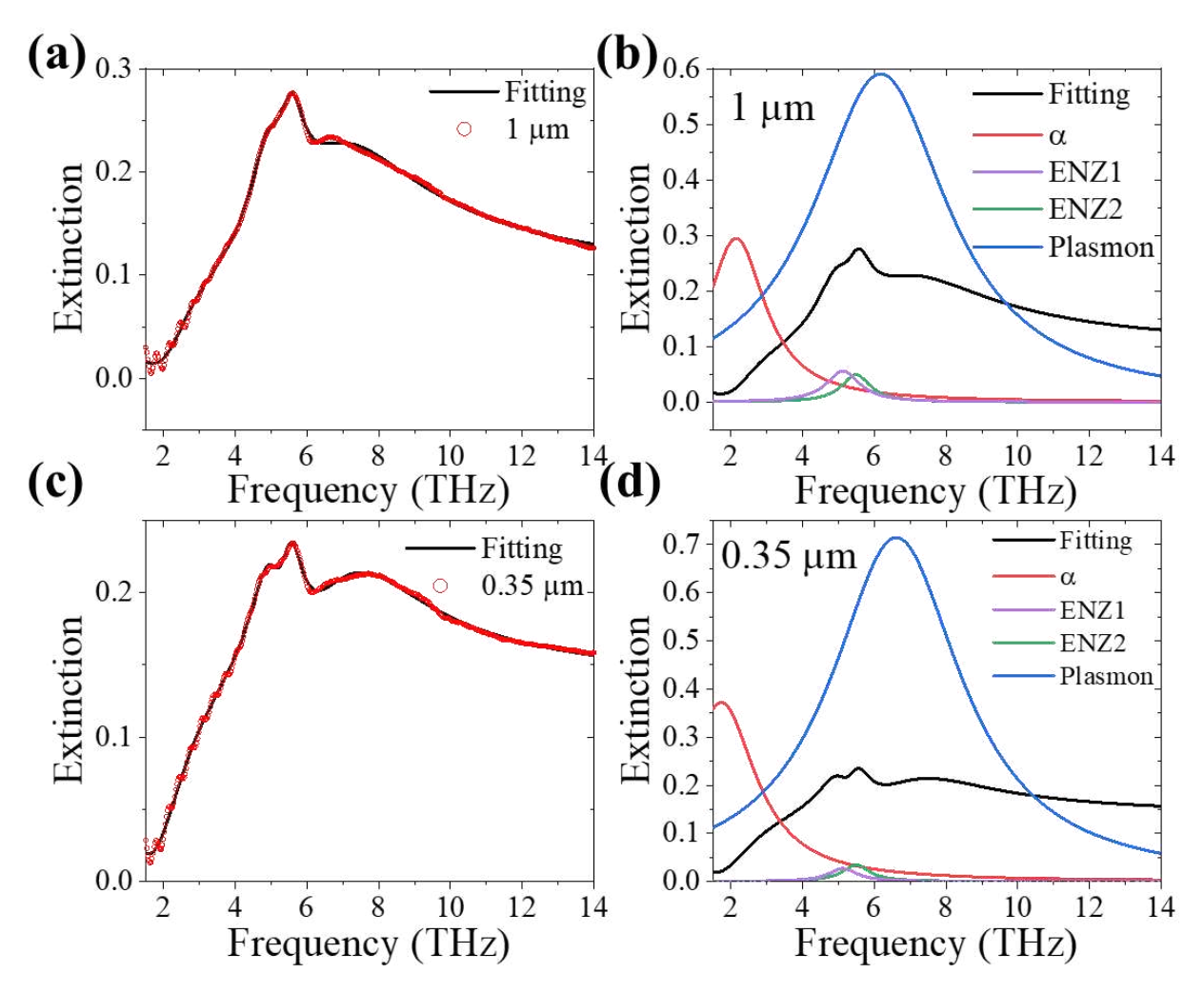


**Figure S8**. Experimental data (red open circles) and independent four-oscillator Fano fitting curve (black solid lines) for samples with a=1 (a) and  $0.35 \,\mu\text{m}$  (c). Individual oscillators extracted from the Fano fitting process for samples with a=1 (b) and  $0.35 \,\mu\text{m}$  (d). Red, violet, green, and blue curves are the  $\alpha$  phonon, BIS ENZ1 mode, ENZ2 mode, and plasmon mode, respectively. The black curves are the Fano fitting curves from (a, c).

# VII. Substrate transmission comparison

In Fig. S9, the raw transmission data for the silicon and sapphire substrates is shown. This data is unnormalized, thus showing the relative responsiveness of the source, beamsplitter, and detector in the FTIR as well as comparing the relative transmission of each substrate.

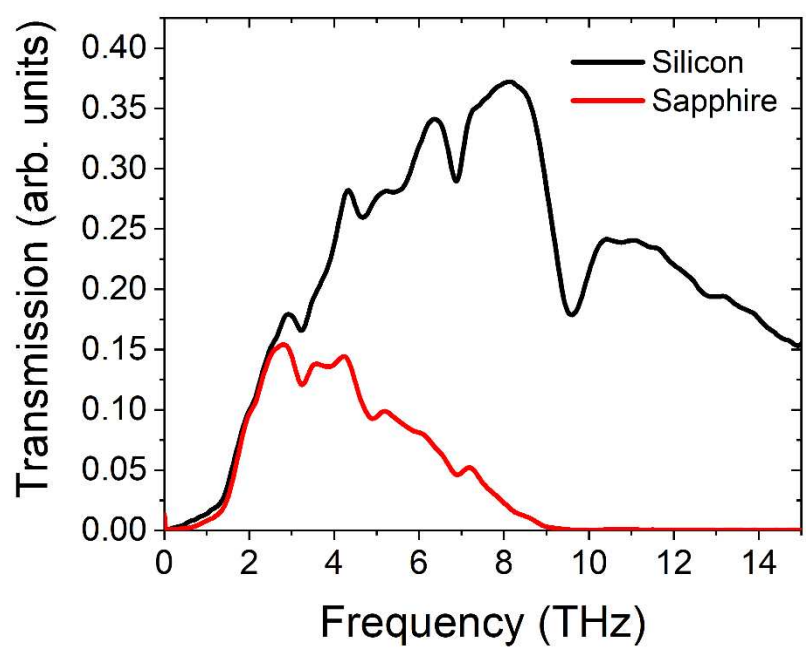


**Figure S9**. Transmission through the silicon substrate (black) and sapphire substrate (red). Data was taken for both samples using the same FTIR configuration. Data is unnormalized.

# **VIII.** Fitting Parameter Tables

**Table S1.** Fitting parameters for the five-oscillator model for the 5L-50nm sample on silicon in the main text.  $a_r$  is a background parameter,  $\omega$ , b,  $\gamma$ , and  $\varphi$  represent the frequency, strength, linewidth, and phase of the oscillators, respectively.  $\alpha$ , BIS $\beta$ , and BS $\beta$  represent the  $\alpha$  phonon of the system, the  $\beta$  phonon of BIS, and the  $\beta$  phonon of Bi<sub>2</sub>Se<sub>3</sub>, respectively. e1 and e2 represent the ENZ1 and ENZ2 modes of BIS, respectively. v0, v1, and v2 represent the VPP0, VPP1, and VPP2 modes of the HMM. Q indicates the quality factor and  $n^*$  the mode index of the VPP modes.

	3 μm		1 μm	0.66 μm	0.5 μm	0.35 μm		0.25 μm
$a_{r}$	0.30917	$a_{r}$	0.277941	0.263531	0.271318	0.225	$a_{r}$	0.432525
ω-α	1.96284	ω-α	1.97324	2.06398	2.03902	2.033	ω-α	1.9915
b-α	0.231025	b-α	0.401679	0.409229	0.118049	0.473457	b-α	0.17302
γ-α	0.462118	γ-α	0.477794	0.495348	0.471893	0.485169	γ-α	0.30545
φ-α	3.57034	φ-α	2.96042	3.66412	3.65271	3.72014	φ-α	4.11756
b-BISβ	1.19057	b-v1	0.496814	0.630589	0.731233	0.810825	b-v2	0.413989
γ-BISβ	1.12972	γ-v1	1.44008	2.95958	2.69321	3.18566	γ-v2	1.81939
φ-BISβ	1.96824	φ-v1	1.96096	2.07987	1.96959	2.52297	φ-v2	1.06845
ω-ΒΙSβ	4.56578	ω-v1	6.34245	6.5076	6.80682	7.76368	ω-v2	7.07739
b-v0	1.0924	b-v0	0.345351	0.187181	0.140274	0.509136	b-v1	0.579945
γ-ν0	0.80777	γ-ν0	2.30501	3.71421	2.7988	3.68344	γ-v1	2.11654
φ-ν0	0.473447	φ-ν0	1.46007	1.25789	0.695295	0.820463	φ-v1	1.84943
ω-ν0	5.46832	ω-ν0	7.41594	8.3873	8.87475	9.44448	ω-v1	8.4093
b-e2	0.797867	b-e2	0.243227	0.287767	0.294475	0.305633	b-e2	0.080687
γ-e2	0.699407	γ-e2	0.436812	0.468487	0.499999	0.499976	γ-e2	0.726685
φ-e2	3.70491	ф-е2	1.236	1.40072	1.19254	0.873475	ф-е2	1.41368
ω-e2	5.52906	ω-e2	5.52197	5.5352	5.45773	5.40738	ω-e2	5.59218
b-BSβ	0.304859	b-e1	0.333759	0.265795	0.259914	0.285452	b-BISβ	0.057197
γ-BSβ	0.673268	γ-e1	0.615	0.491162	0.499595	0.494742	γ-BISβ	0.556848
φ-ΒSβ	3.14663	φ-e1	2.60082	3.63363	3.21614	3.14106	φ-BISβ	0.372285
ω-ΒSβ	3.90035	ω-e1	5.18663	5.31168	5.20609	5.19921	ω-BISβ	4.41921
Q-v0	6.7	Q-v0	3.22	2.25	3.17	2.56	Q-v1	3.98
		Q-v1	4.40	2.19	2.52	2.44	Q-v2	3.88
n*-v0	55	n*-01	126	167	211	283	n*-v1	445

n*-v1 147 215 276 345 n*-v2 531
---------------------------------

**Table S2.** Fitting parameters for the five-oscillator model for the 5L-50nm sample on sapphire shown in Section IX of the Supporting Information.  $a_r$  is a background parameter,  $\omega$ , b,  $\gamma$ , and  $\phi$  represent the frequency, strength, linewidth, and phase of the oscillators, respectively.  $\alpha$ , BIS $\alpha$ , BIS $\beta$ , and BS $\beta$  represent the  $\alpha$  phonon of Bi<sub>2</sub>Se<sub>3</sub>, the  $\alpha$  phonon of BIS, the  $\beta$  phonon of BIS, and the  $\beta$  phonon of Bi<sub>2</sub>Se<sub>3</sub>, respectively. e1 and e2 represent the ENZ1 and ENZ2 modes of BIS, respectively. v0 and v1 represent the VPP0 and VPP1 modes of the HMM, respectively.

	3um	0.66um		1um		0.5um		0.25um		0.35um
a	0.03	0.18552	ar	0.44346	ar	0.39586	ar	0.59785	ar	0.36704
ω-α	1.95957	1.99387	ω-α	1.97516	ω-α	1.98131	ω-α	1.99816	ω-α	2.01222
b-α	0.28974	0.35547	b-α	0.47503	b-α	0.075	b-α	1.4609	b-α	1.0929
γ-α	0.45819	0.79588	γ-α	0.85857	γ-α	0.85464	γ-α	0.20682	γ-α	0.23562
φ-α	2.76846	2.25161	φ-α	1.96626	φ-α	2.59956	φ-α	1.90624	φ-α	2.45136
b-e1	0.31766	0.14702	b- BISβ	0.25494	b- BISβ	0.13536	b-e1	0.09963	b-e1	0.20098
γ-e1	0.68007	0.43256	γ- BISβ	0.71672	γ- BISβ	0.6495	γ-e1	0.45515	γ-e1	0.54507
φ-e1	1.28867	0.37737	φ- BISβ	1.86329	φ- BISβ	2.09087	φ-e1	1.23138	φ-e1	1.50583
ω-e1	4.74413	4.9608	ω- BISβ	4.22086	ω- BISβ	4.10145	ω-e1	4.83473	ω-e1	4.78514
b-e2	0.31658	0.83061	b-e2	1.32181	b-e2	1.14021	b-e2	1.19204	b-e2	1.14943
γ-e2	0.8054	0.34814	γ-e2	0.27337	γ-e2	0.25503	γ-e2	0.58288	γ-e2	0.51454
φ-e2	0.97119	2.32263	φ-e2	1.77126	φ-e2	1.76364	φ-e2	1.36487	φ-e2	2.14217
ω-e2	5.29969	5.74075	ω-e2	5.75116	ω-e2	5.73294	ω-e2	5.53556	ω-e2	5.43054
b-v0	0.25765	0.65549	b-v1	1.24651	b-BSβ	0.17049	b- BISα	0.04201		
γ-ν0	1.43565	1.59204	γ-v1	0.33003	γ-ΒSβ	0.8943	γ- BISα	0.42552		
φ-v0	1.28285	0.72322	φ-v1	0.64331	φ-ΒSβ	3.89036	φ- BISα	4.61584		
ω-ν0	6.7866	8.51659	ω-v1	6.58134	ω- BSβ	3.68352	ω- BISα	2.67179		
b-BSβ	0.16729	0.04194	b-BSβ	0.23897						
γ-BSβ	0.6485	0.66091	γ-ΒSβ	0.88327						
φ-ΒSβ	0.9052	1.69893	φ-BSβ	3.1896						
ω- BSβ	3.72582	3.87308	ω- BSβ	3.66316						

#### IX. Permittivity models

To model our structure, we need to model the permittivity of the individual layers. For the sapphire substrate, we used the following

$$\varepsilon_{Al_2o_3}(\omega) = n_0^2 + (n_0^2 - 1)(\lambda\omega)^2 + i\gamma(n_0^2 - 1)(\lambda\omega)$$
 (S1)

where  $n_0 = 3.2$ ,  $\lambda = 20.4 \times 10^{-4}$  cm, and  $\gamma = 0.036.^8$  For the silicon substrate, we used a constant permittivity of 11.67. For the Bi<sub>2</sub>Se<sub>3</sub> layers, we used

$$\varepsilon_{Bi_2Se_3}(\omega) = 1 + \frac{S_\alpha^2}{\omega_\alpha^2 - \omega^2 - i\omega\gamma_\alpha} + \frac{S_\beta^2}{\omega_\beta^2 - \omega^2 - i\omega\gamma_\beta}$$
 (S2)

with  $\omega_{\alpha} = 63.03 \text{ cm}^{-1}$ ,  $S_{\alpha} = 675.9 \text{ cm}^{-1}$ ,  $\gamma_{\alpha} = 17.5 \text{ cm}^{-1}$ ,  $\omega_{\beta} = 126.94 \text{ cm}^{-1}$ ,  $S_{\beta} = 100 \text{ cm}^{-1}$ ,  $\gamma_{\beta} = 10 \text{ cm}^{-1}$ . For the BIS layers, we used

$$\varepsilon_{BIS}(\omega) = \varepsilon_{\infty, \frac{p}{S}} + \frac{S_{\alpha}^{2}}{\omega_{\alpha}^{2} - \omega^{2} - i\omega\gamma_{\alpha}} + \frac{S_{\beta}^{2}}{\omega_{\beta}^{2} - \omega^{2} - i\omega\gamma_{\beta}}$$
 (S3)

where  $\varepsilon_{\infty,p} = 10.26$ ,  $\varepsilon_{\infty,s} = 7.40$ ,  $\omega_{\alpha} = 88.98$  cm<sup>-1</sup>,  $S_{\alpha} = 366.02$  cm<sup>-1</sup>,  $\gamma_{\alpha} = 60.50$  cm<sup>-1</sup>,  $\omega_{\beta} = 142.38$  cm<sup>-1</sup>,  $S_{\beta} = 188.39$  cm<sup>-1</sup>,  $\gamma_{\beta} = 22.39$  cm<sup>-1</sup>. Finally, the optical conductivity of the TI surface states is given by  $^{10-12}$ 

$$\sigma = \frac{e^2 E_F}{\hbar^2 4\pi} \frac{i}{\omega + i\tau^{-1}} \tag{S4}$$

$$E_F = \hbar k_F v_F \tag{S5}$$

$$n = \frac{g_s g_v}{4\pi} k_F^2 \tag{S6}$$

$$\tau = \frac{\mu_m E_F}{e v_F^2} \tag{S7}$$

where  $E_F$  is the Fermi energy of the surface states and  $\tau$  is the relaxation time. For our TI films, the sheet carrier concentration at room temperature  $n_{2D} = 2n_D = 1 \times 10^{13}$  cm<sup>-2</sup> and the mobility is  $\mu_m \approx 600 \text{ cm}^2 \text{V}^{-1} \text{s}^{-1}$ . We attribute the majority of carriers to the surface states. We therefore get  $E_F \approx 260 \text{ meV}$  above the Dirac point and  $\tau \approx 0.06 \text{ ps}$ .

# X. HMM grown on sapphire

To support our claim that the superlattice is acting like an HMM, we can look at data for a superlattice grown on a sapphire substrate. 5L-50 nm multilayer films are directly deposited on a 0.5 mm thick, 1 cm×1 cm sapphire substrate at 300 °C and patterned into ribbon structures with widths a=3, 1, 0.66, 0.5, 0.35 and 0.25 µm. The extinction spectra for these samples are shown in Figure S10(a) where the open, colored symbols are the experimental data points, and the black lines are the Fano fitting. In the Fano fitting, we used the minimum number of oscillators to obtain a good fit, and we confine their frequencies to a small range except for the oscillators associated with the VPP modes. For example, if an extinction spectrum could be fit equally well using two VPP modes or using three VPP modes, we preferred the fit using only two VPP modes to avoid overfitting the data. The extracted resonances are overlaid on the color plot generated with TMM modeling in **Figure S10**(b). For samples with a=3, 1, and 0.66 μm, we need only one VPP mode oscillator to fit the data. The resulting mode frequencies for the a=3 and 0.66 µm samples fall on the dispersion curve for VPP0, while the frequency for the a=1 µm sample falls on the dispersion curve for VPP0. For samples with narrower ribbon width, we do not clearly see a peak in the extinction spectra, so we only fit the data with the non-dispersive polariton modes. We attribute our inability to clearly observe multiple VPP modes in this sample to the narrow transparency window of sapphire in this frequency range. The transmission through our sapphire substrates begins to decrease around 7 THz which makes it challenging to distinguish multiple points for VPP0 and VPP1. In addition, the smaller transparency of sapphire compared to silicon makes it difficult to pick out weaker modes such as VPP3. Despite these challenges, these data support our argument that this type of superlattice acts as a Dirac HMM in the THz. If we compare the experimental extinction curves shown in Figure 2 and Figure 3 in the main text, we see a close resemblance in the shape of curves for samples with the same ribbon widths. This consistency matches our expectation that structurally similar samples should show similar extinction spectra and further confirms that we are observing VPP modes in a Dirac HMM.

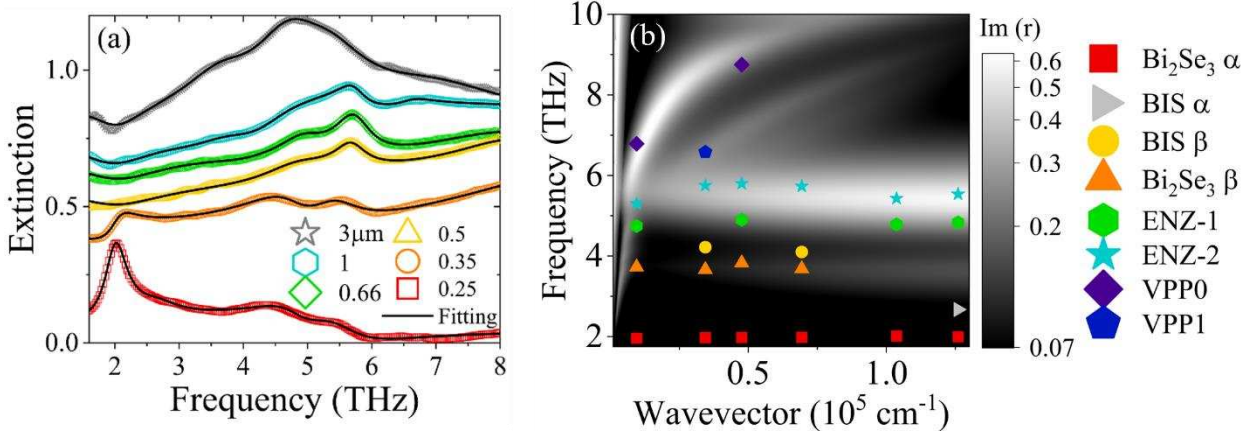


**Figure S10**. (a) Fano fitting curves (black) for the TM extinction spectra (colored symbols) of the 5L-50nm HMM grown on sapphire. The data are offset for better visualization. (b) Transfer matrix modeling of the 5L-50nm Bi<sub>2</sub>Se<sub>3</sub>-BIS HMM shown in grayscale. Data points are the corresponding mode frequencies extracted from the Fano fitting.

# **XI.** Effect of number of layers

We have performed effective medium theory calculations for Bi<sub>2</sub>Se<sub>3</sub>-BIS Hyperbolic metamaterial for periods 1 through 8. We can see from **Figure S11** that the requirement Real( $\varepsilon_{\perp}$ ) > 0 is met at all periods within the intended frequency range of 5 to 10 THz. However, the frequency range that satisfies the second condition to form hyperbolic media, Real( $\varepsilon_{||}$ ) < 0, expands as the number of periods increases and converges to the range 5-10 THz after five periods. Hence, we selected the period five as the optimal choice for our samples.

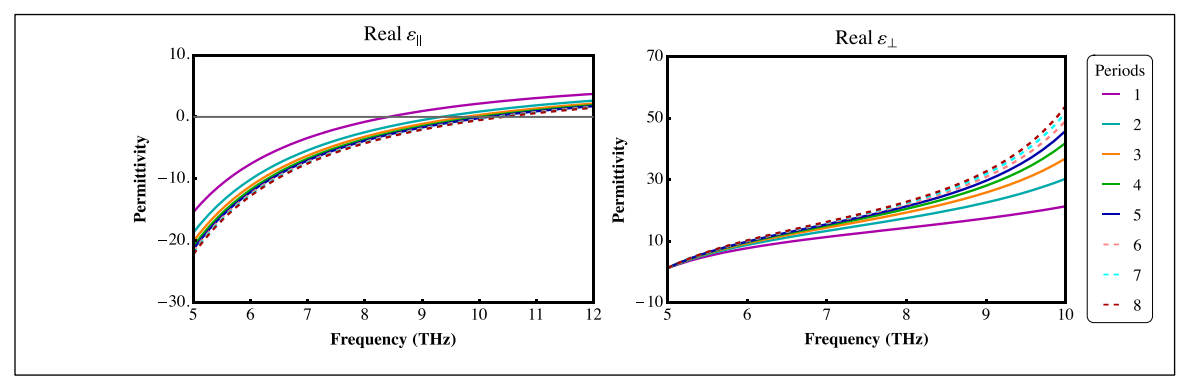


**Figure S11.** Parallel and perpendicular components of permittivity for Bi<sub>2</sub>Se<sub>3</sub>-BIS Hyperbolic metamaterial calculated using effective medium theory for periods 1 through 8. Here we have considered the thickness of each layer to be 50 nm.

Further, from **Fig. 2(b)** and **Fig. 3(b)**, of the main manuscript we observe that VPP0 and VPP1 modes are supported between the range 5-10 THz for ribbon widths varying from 0.25 to 3  $\mu$ m. If the number of periods is lower than five, both VPP modes are supported only at larger ribbon widths. For example, for a structure with period four, the condition to form hyperbolic media is satisfied only in the range 5-9 THz. Hence, one has to choose the ribbon width greater than 0.5  $\mu$ m to support both VPP0 and VPP1 modes.

#### **Reference:**

- (1) Shekhar, P.; Atkinson, J.; Jacob, Z. Hyperbolic Metamaterials: Fundamentals and Applications. *Nano Converg.* **2014**, *1* (14), 1–17. https://doi.org/10.1186/s40580-014-0014-6
- (2) Wang, Z.; Ginley, T. P.; Mambakkam, S. V.; Chandan, G.; Zhang, Y.; Ni, C.; Law, S. Plasmon Coupling in Topological Insulator Multilayers. *Phys. Rev. Mater.* **2020**, *4* (11), 115202. https://doi.org/10.1103/PhysRevMaterials.4.115202.
- (3) Brahlek, M.; Bansal, N.; Koirala, N.; Xu, S.-Y.; Neupane, M.; Liu, C.; Hasan, M. Z.; Oh, S. Topological-Metal to Band-Insulator Transition in (Bi1-xInx)2Se3 Thin Films. *Phys. Rev. Lett.* **2012**, *109* (18), 186403. https://doi.org/10.1103/PhysRevLett.109.186403.
- (4) Dordevic, S. V.; Wolf, M. S.; Stojilovic, N.; Lei, H.; Petrovic, C. Signatures of Charge Inhomogeneities in the Infrared Spectra of Topological Insulators Bi2Se3, Bi2Te3 and Sb2Te3. *J. Phys. Condens. Matter* **2013**, 25 (7), 075501. https://doi.org/10.1088/0953-8984/25/7/075501.
- (5) Di Pietro, P.; Vitucci, F. M.; Nicoletti, D.; Baldassarre, L.; Calvani, P.; Cava, R.; Hor, Y. S.; Schade, U.; Lupi, S. Optical Conductivity of Bismuth-Based Topological Insulators. *Phys. Rev. B* **2012**, *86*, 045439. https://doi.org/10.1103/PhysRevB.86.045439.

- (6) Post, K. W.; Chapler, B. C.; Liu, M. K.; Wu, J. S.; Stinson, H. T.; Goldflam, M. D.; Richardella, A. R.; Lee, J. S.; Reijnders, A. A.; Burch, K. S.; Fogler, M. M.; Samarth, N.; Basov, D. N. Sum-Rule Constraints on the Surface State Conductance of Topological Insulators. *Phys. Rev. Lett.* 2015, 115 (11), 116804. https://doi.org/10.1103/PhysRevLett.115.116804.
- (7) Aguilar, R. V.; Stier, A. V.; Liu, W.; Bilbro, L. S.; George, D. K.; Bansal, N.; Wu, L.; Cerne, J.; Markelz, A. G.; Oh, S.; Armitage, N. P. Terahertz Response and Colossal Kerr Rotation from the Surface States of the Topological Insulator Bi 2 Se 3. https://doi.org/10.1103/PhysRevLett.108.087403.
- (8) Roberts, S.; Coon, D. D. Far-Infrared Properties of Quartz and Sapphire. *J. Opt. Soc. Am.* **1962**, *52* (9), 1023. https://doi.org/10.1364/JOSA.52.001023.
- (9) Wollack, E. J.; Cataldo, G.; Miller, K. H.; Quijada, M. A. Infrared Properties of High-Purity Silicon. *Opt. Lett.* **2020**, *45* (17), 4935–4938. https://doi.org/10.1364/OL.393847.
- (10) Li, L. L.; Xu, W.; Peeters, F. M. Optical Conductivity of Topological Insulator Thin Films. *J. Appl. Phys.* **2015**, *117* (17), 175305. https://doi.org/10.1063/1.4919429.
- (11) Parhizgar, F.; Moghaddam, A. G.; Asgari, R. Optical Response and Activity of Ultrathin Films of Topological Insulators. *Phys. Rev. B* **2015**, *92* (4), 045429. https://doi.org/10.1103/PhysRevB.92.045429.
- (12) Xiao, X.; Wen, W. Optical Conductivities and Signatures of Topological Insulators with Hexagonal Warping. *Phys. Rev. B* **2013**, 88 (4), 045422. https://doi.org/10.1103/PhysRevB.88.045442.